

Al-based Plasmonic Nanoparticles as an Alternative to Noble Metal Plasmonics

A THESIS

Submitted by

Arvind Pujari

for the award of the degree

of

BACHELORS OF TECHNOLOGY



**DEPARTMENT OF METALLURGICAL AND MATERIALS
ENGINEERING**

**INDIAN INSTITUTE OF TECHNOLOGY MADRAS
CHENNAI-600036**

May 2020

THESIS CERTIFICATE

This is to certify that the thesis entitled "**Al-based Plasmonic Nanoparticles as an Alternative to Noble Metal Plasmonics**" submitted by **Arvind Pujari** to the Indian Institute of Technology, Madras for the award of the degree of **Bachelors of Technology** is a bona fide record of research work carried out by him under my supervision. The contents of this thesis, in full or in parts, have not been submitted to any other Institute or University for the award of any degree or diploma.

Dr Tiju Thomas
Associate Professor
Department of Metallurgical and Materials Engineering
Indian Institute of Technology Madras
Chennai – 600 036.

Place: Chennai

Date: May 2020

ACKNOWLEDGEMENTS

I would like to thank my parents and friends for their unwavering support throughout the course of this project. I would also like to thank my guide, Dr. Tiju Thomas, for showing immense faith in me, and answering even the most trivial of my questions. Lastly, I would like to thank the IIT M CC for providing access to the COMSOL Multiphysics Software.

ABSTRACT

Keywords: Plasmonics, Core-Shell Nanoparticles, Nanocubes, Light Harvesting, Peak Shifting, Effective Medium Theory, Light Trapping, Alloy Nanoparticles, Transfer Matrix Method

Plasmonic nanoparticles have been used for a variety of applications, including light trapping in thin film solar cells. The most commonly used metals for this are Au, Ag and Al, however Au and Ag are expensive, while Al is susceptible to environmental corrosion. We offer two alternatives.

The first, is to alloy Al with other metals: especially other earth abundant plasmonic metals. This offers plasmonic tunability and improved corrosion resistance. In this report we study the light trapping ability of Al-Cu, Al-Au, Al-Ni, Al-In and Al-Mg alloys in an amorphous silicon solar cell. We use a combination of Mie Theory, Transfer Matrix Modelling and Effective Medium Theory to develop a simple numerical solution to this problem. Al-In and Al-Mg alloy nanoparticles emerge as the most suitable candidates for this application. Al (75%) In (25%) nanoparticles of size 22nm are shown to improve the absorption of amorphous silicon by 28%.

The second is coating Al with a thin shell of another metal. New reports on the stabilization of Al(0) in water by coating it with a thin Cu shell have opened up a fresh avenue to explore corrosion resistant aluminum plasmonics. However, the effect of a Cu shell on the plasmonic properties of Al is hitherto unknown and needs to be understood. Moreover, almost all studies have been carried out on the optical properties of Al-core metallic-shell nanoparticles. Hence, for the first time, we report here a study on the absorption and scattering cross-sections of Al-Cu core shell nanoparticles (spheres, cubes, cuboids and their dimers in a variety of orientations, with a characteristic dimension between 50-100nm) under an illumination of 300-900nm. Notably, the addition of a 10nm Cu shell shifts the scattering peak of a 100nm Al nanosphere from 390nm to 590nm. The peak absorption and scattering wavelengths of core-

shell nanocubes increase almost linearly with shell thickness. The effect of oxidation of the Cu shell is shown to be negligible. Thus, a Cu shell seems to improve the plasmonic performance of Al.

Therefore, we hope that this report will spur further interest into the utility of Al-alloy and Al-Cu core-shell nanoparticles for plasmonic applications.

TABLE OF CONTENTS

ABSTRACT	4
TABLE OF CONTENTS	6
LIST OF FIGURES	7
<i>Chapter 1: Introduction</i>	12
1.1. Introduction	12
1.2. Objective of the Work	13
<i>CHAPTER 2 : Literature Review</i>	14
2.1. Background	14
2.2. Problem Definition and Approach	17
<i>CHAPTER 3 : Methods and Techniques</i>	19
<i>CHAPTER 4 : Results and Discussion: Al-Cu Core-Shell Applications</i>	30
<i>CHAPTER 5 : Results and Discussion: Al-M Alloy Nanoprticles</i>	41
<i>CHAPTER 6 : Summary and Conclusions</i>	55
References	58

LIST OF FIGURES

Figure 2-1 Light matter interaction for a plasmonic nanosphere. The electrons naturally oscillate with a frequency known as the plasma frequency. When the frequency of incident light matches the plasma frequency, localized surface plasmon resonance (LSPR) occurs....14

Figure 2-2 Light trapping in thin film solar cells using plasmonic nanoparticles. By increasing the path length of light using plasmonic scatterers, the semiconductor absorbs a greater proportion of the incident light.16

Figure 3-1 (a) Geometry used for simulations. A PML can be used to truncate the computational region to a sphere of radius ~ 200-400nm. (b) The normalized scattering cross sections of 50nm and 100nm Al nanospheres. A scattering peak exists only for the 100nm nanosphere in the visible region. The Mie Scattering Solutions are in close agreement with the FEM analysis.20

Figure 3-2 (a) n and (b) k values for Cu, Au, Ni, In and Mg in the visible-NIR range (300-900nm). Cu and Au show similar variation in n and k values, as do Mg and In. Therefore, it may be expected that their optical responses are similar.24

Figure 3-3. The thin film solar cell used for optical simulations. The top and bottom junctions of a:Si (amorphous Silicon) are p and n doped respectively. Since the a:Si layer is so thin, it does not absorb much light. Therefore, plasmonic nanostructures, like the Al-alloy NPs shown here can be added to improve its absorption.....25

Figure 3-4. A summary of the methods used for the calculation of the optical parameters of alloy nanoparticles, and their effect on the absorption by a substrate. Since all the methods used are numerical, the technique is computationally efficient.29

Figure 4-1 Normalized (a) absorption and (b) scattering cross sections of 100nm Au, Cu, Al and Al-Cu core-shell nanospheres. Al@Cu is a better absorber of light than Al, but worse than

Au and Cu. Both Al and Al@Cu show higher scattering cross sections than Au and Cu between 300nm and 500nm.....30

Figure 4-2. Effect of shell thickness on the normalized (a) absorption and (b) scattering cross-sections of 100nm nanospheres. The absorption cross sections monotonically increase with shell thickness. A 10nm shell shifts the scattering peak from 390 to 590nm while slightly decreasing the peak scattering intensity from 3.64 to 3.3.....31

Figure 4-3 Variation of peak normalized scattering intensity and wavelength of a 100nm Al nanosphere with Cu shell thickness. The peak wavelength follows the equation $\lambda_{max} = 391.7 + 12t$ for t between 0 and 9nm and $\lambda_{max} = 550.7 + 4t$ for t between 10nm and 14nm, where t is the thickness of the shell32

Figure 4-4 Comparison of normalized (a) absorption and (b) scattering coefficients of a 100nm Al nanosphere, a 100nm Al cube, and a sphere with the same volume as the cube. Absorption and scattering peaks are seen between 300 and 400nm for a cube, with a 250% and 175% improvement in ABS and SCS respectively w.r.t a sphere at these peaks.33

Figure 4-5 Effect of shell thickness on the normalized absorption and scattering cross-sections of (a) & (b) 50nm and (c) & (d) 100nm nanocubes. The absorption peak shifts from 375nm to 480nm and the scattering peak shifts from 360nm to 660nm when the shell thickness is changed from 0 to 10nm.....34

Figure 4-6 Variation of normalized (a) absorption and (b) scattering intensities and wavelengths of 100nm Al cubes with Cu shell thickness. The normalized absorption peak follows the equation $\lambda_{ABSmax} = 377.4 + 11.91t$ and the normalized scattering peak (the peak with the highest magnitude) follows the equation $\lambda_{SCSmax} = 580 + 8.0t$, where t is the thickness of the Cu shell varying between 2nm and 10nm.....35

Figure 4-7 Variation of (a) absorption and (b) scattering cross sections of three different orientations w.r.t. the xy plane for a nanocuboid with dimensions 50nm, 25nm and 100nm

coated with a 2nm Cu shell. Orientation (b) covers a large part of the solar spectrum between 400 and 700nm.....36

Figure 4-8 Effect of oxide thickness on the normalized (a) absorption and (b) scattering cross section of Al-Cu core-shell nanospheres. A 1nm oxide layer does not produce a perceptible effect on the absorption or scattering curves.37

Figure 4-9 Effect of alloy composition on the (a) absorption and (b) scattering cross sections of 100nm spherical Al-Cu alloys. Increasing Cu content increases the absorption cross section, while a compositional invariance is observed in scattering cross sections for Cu content up to 50%.38

Figure 4-10 (a) Absorption and (b) Scattering cross sections of a variety of dimeric arrangements of a nanocube and nanosphere (both of the same volume). A dimer of two cubes at an angle of 45 degrees with each other (orientation (c)) shows the lowest scattering cross sections ($5.5 \times 10^{-14} \text{ m}^2$) at peak scattering wavelength but the highest absorption cross section ($5.5 \times 10^{-14} \text{ m}^2$) in the 400-800nm range.....39

Figure 4-11 Associated electric fields for configurations (a) to (f) corresponding to Figure 11 at a wavelength of 670nm.40

Figure 5-1 Weighted (a) scattering efficiencies and (b) scattering ratios for Al alloyed with five different metals, as a function of their radii and volume fraction of Al. *Qscaratio – weighted* is 0.76 for a 50% ($f_{\text{Al}}=0.5$) Al-Mg alloy of radius 60nm ($R_{\text{NP}}=60\text{nm}$), as opposed to 0.74, 0.63, 0.71 and 0.7 for Al-In, Al-Ni, Al-Au and Al-Cu NPs respectively, with the same composition and radius. Thus, Al-In and Al-Mg display the best scattering behavior at a given f_{Al} and R_{NP}42

Figure 5-2. Weighted (a) absorption efficiencies and (b) absorption ratios for Al alloyed with five different metals, as a function of their radii and volume fraction. *Qabsratio – weighted* is 0.894 for a 50% Al-Ni alloy of radius 20nm, as opposed to 0.79, 0.77, 0.85 and

0.86 for Al-In, Al-Mg, Al-Au and Al-Cu NPs respectively, with the same composition and radius. Thus, Al, Al-Au, Al-Cu and Al-Ni display the best absorption behavior at a given f_{Al} and R_{NP}43

Figure 5-3. Extinction as a function of wavelength for different nanoparticle sizes and alloy compositions. For $R_{NP}=15\text{nm}$, the resonant wavelengths lie in the 100-200nm range, as shown in the inset figures (a) and (b). For larger nanoparticles ($R_{NP}=75\text{nm}$), as seen in (c) and (d), the resonant peaks exist in the visible-NIR (300-900nm) region, and multipolar contributions to the extinction can be seen eg. Al-Mg ($f_{Al}=75\%$) in (c). The electric fields corresponding to the marked resonant wavelengths in (b) and (d) are shown in (e). For Al-rich alloys ((b) and (d)), the extinction curves converge, which means that they will show a similar optical response.45

Figure 5-4. The power absorbed by a:Si, weighted by the AM1.5G solar spectrum, relative to the power absorbed by a:Si. Al-In and Al-Mg alloys The maximum absorption enhancement of the a:Si layer increases with increasing surface coverage (1.04 for Al-Mg when $F=0.15$ to 1.28 for Al-Mg when $F=0.6$) However the wavelength at which the maximum occurs decreases with increasing F . Al-In and Al-Mg show a high (>20%) absorption enhancement for a:Si for a wide alloy composition.....46

Figure 5-5. The fraction of light absorbed by a:Si with varying incident angles of incident light, relative to the light absorbed by bare Si, for a fixed surface coverage($F=0.6$) for different values of R_{NP} and f_{Al} . (b) shows that when $f_{Al}=75\%$, the NPs show better angular absorption than in (a) where $f_{Al}=25\%$ for AOI between 0 and 54 degrees. (a) and (b) ($R_{NP}=20\text{nm}$) show a wider range of enhancement (>1) than (c) and (d) ($R_{NP}=40\text{nm}$).48

Figure 5-6. The fraction of incident power absorbed by a:Si vs wavelength for Al (75%)-M (25%) alloys. Al, (Al-75% Mg-25%) and (Al-75% In-25%) improve the absorption of a:Si to the maximum extent (29%, 28% and 28% respectively). Thus, a small amount of alloying of Al NPs with these metals does not affect their light trapping efficiency much.....50

Figure 5-7. (a) The variation between the surface coverage (F) and the optimum radius for an alloy with 75% Al and 25% In. A decreasing linear relation is seen: as F increases, R_{NP} decreases linearly. (b) The variation between the fraction of incident light absorbed by a:Si and the R_{NP} for the same alloy described in part (a). The graph clearly shows that there is a “optimum” radius for each F for maximum light absorption.51

Figure 5-8. The absorption of a:Si as a function of wavelength for different surface coverages for an Al alloy with 75% In.. For each value of F , the radius of the NPs were taken as $R_{optimum}$, which was calculated earlier. The improvement due to the presence of the Al-In NPs is marked in the figure. When $F=0.6$, the presence of Al-In NPs of size 22nm results in a 28% increase in a:Si absorption relative to a:Si without NPs, and a 13% increase in a:Si absorption relative to a:Si with Ag NPs of the same radius placed on it.....52

Figure 5-9. We consider Gaussian distributions of Al-In NP radii ($f_{Al}=75\%$), centred around the $R_{optimum}$ for each value of the surface coverage, F . The distributions are shown in the inset figure. For $F=0.6$, for a narrow distribution ($SD=1$), an enhancement of 27% is seen vs bare a:Si. For a flatter distribution ($SD=5$), an enhancement of 21% is seen vs bare a:Si.53

Chapter 1: Introduction

1.1. Introduction

Plasmonic materials have long been of interest due to their applications in photovoltaics [1], [2], cancer therapy [3], photocatalysis [4], desalination [5] and optoelectronic [6] devices. The most common plasmonic materials used currently are gold [7] and silver [8], due to their efficient plasmonic behavior in the visible light region (400-700nm). However, the plasmonic response of Au is inhibited due to dissipative channels which emerge due to interband transitions at wavelengths less than 550nm [9], while Ag suffers from environmental corrosion. Moreover, the cost and rarity of these noble metals make their utilization prohibitively expensive, and scalability nearly impossible. Therefore, there is an increasing need to look beyond noble metals [10] for sustainable, large scale applications of plasmonic materials.

Aluminum has long been touted as a replacement for gold and silver in plasmonic applications due to its low cost, earth abundancy and ease of processing [11]. The interband transitions in aluminum occur at about 800nm, which allows plasmonic tuning over the entire UV-Vis spectrum [12]. Aluminum scatterers have been explored for applications such as light trapping in solar cells [13], while a periodic array of Al nanoparticles in an Anodized Aluminum Oxide (AAO) membrane is shown to have an excellent photothermal efficiency for desalination applications [14]. Likewise, Al on CuO has been investigated as a photothermal absorber [15]. Therefore, arguably aluminum represents the best opportunity for scalable plasmonic applications. However, aluminum spontaneously corrodes upon contact with oxygen, forming an oxide layer which can severely impair plasmonic response [16]. This has so far restricted the large-scale utilization of aluminum as a viable alternative to gold and silver as a plasmonic material.

In this work, we look at two sets of Al-based nanoparticles: Al-Cu core-shell nanoparticles and Al-based alloy nanoparticles. We investigate their plasmonic properties and suitability for plasmonic applications using a combination of FEM analysis and Mie Scattering solutions. We therefore show which material compositions are the most suitable to replace noble metal plasmonics.

1.2. Objective of the Work

1. To undertake a comprehensive computational study of Al@Cu core-shell sphere, cubes and cuboids as well as Al-Cu alloy systems, to investigate the plasmonic utility of these systems
2. To carry out studies on the light trapping efficiency in an amorphous thin film solar cell due to plasmonic Al alloy nanoparticles.
3. To compare and contrast these results with existing, noble metal based plasmonic solutions

Hence, we seek to demonstrate that Al-based plasmonics may offer an alternative to existing noble metal plasmonics.

CHAPTER 2 : Literature Review

2.1. Background

Plasmonic nanoparticles are particles whose electron density can couple with electromagnetic radiation of wavelengths that are far larger than the particle due to the nature of the dielectric-metal interface between the medium and the particles: unlike in a pure metal where there is a maximum limit on what size wavelength can be effectively coupled based on the material size.

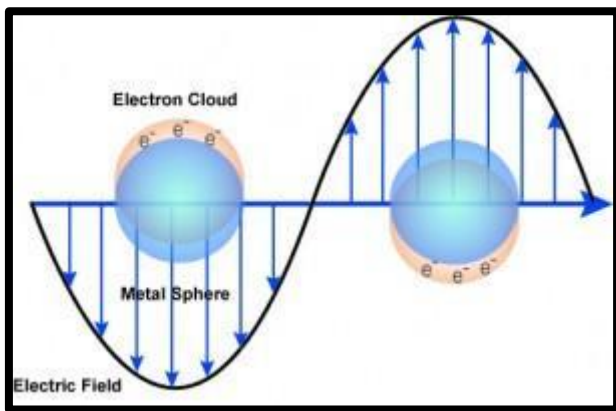


Figure 2-1 Light matter interaction for a plasmonic nanosphere. The electrons naturally oscillate with a frequency known as the plasma frequency. When the frequency of incident light matches the plasma frequency, localized surface plasmon resonance (LSPR) occurs.

Plasmonic nanoparticles have been used for a variety of applications such as biosensing [17], communication [18], cancer therapy [19] and solar cell applications [20]. The most commonly used plasmonic metals are gold and silver. However, the plasmonic response of Au is inhibited due to dissipative channels due to the presence of interband transitions at wavelengths less than 550nm [21] , while Ag suffers from environmental corrosion [22]. This, along with their prohibitive costs will continue to be an impediment to the wide scale utilization of plasmonic nanomaterials.

It is for this reason that there has been intense research on developing alternate plasmonic materials. These include Al [23], Ni [24], Cu [25], In [26] and Mg [27]. These metals are

significantly more earth abundant and hence, cheaper than Au and Ag. Al, In and Mg exhibit strong LSPR in the UV region. Moreover, Al, Mg and In exhibit interband transitions at 820nm [28], 1750nm [29] and 880nm [30] respectively, which lies at the edge, or beyond the visible region (300-700nm). Thus, these metals can support a wide spectral range of surface plasmons below their interband frequency. Additionally, Cu displays optical constants similar to Au [31], and hence display similar optical properties to Au, but is far more earth abundant.

An area which has seen an increased use of plasmonic nanoparticles is plasmonic light trapping, especially in thin film solar cells [32]. Thin film solar cells use hydrogenated amorphous silicon, which can be deposited using PECVD, leading to a much lower manufacturing cost [33]. Additionally, amorphous silicon layers can be made much thinner [34] than crystalline silicon layers. This, coupled with the fact that amorphous silicon can be deposited on plastic due to low deposition temperatures [35] makes it useful for flexible and wearable electronics. Additionally, its low cost implies that it is more suitable for economics of scale. However, due to the small thickness of the amorphous silicon layer used, such thin film solar cells are rather inefficient [36]. It is in this connection that plasmonic nanoparticles can be used to trap light inside the silicon layer, leading to enhanced absorption, as shown in Figure 2-2

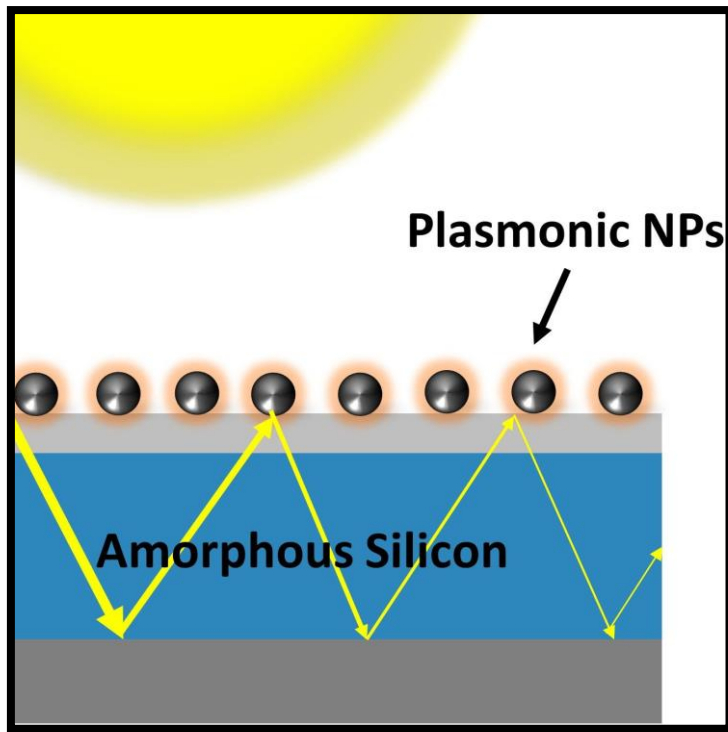


Figure 2-2 Light trapping in thin film solar cells using plasmonic nanoparticles. By increasing the path length of light using plasmonic scatterers, the semiconductor absorbs a greater proportion of the incident light.

While most of the research conducted on plasmonic light trapping has utilized Au and Ag [37] [38], there have been some reports into the utility of Al nanoparticles [39] for these applications. However, Al nanoparticles are difficult to synthesize [40], difficult to size focus [41], and are particularly prone to environmental corrosion which has a detrimental effect on the plasmonic properties of Al [23]. It is in this connection that Al alloy nanoparticles and nanocomposites (i.e. heterogeneous Al alloys), particularly alloys of Al with the earth abundant plasmonic metals mentioned earlier are useful. This is because such alloys tend to show improved corrosion resistance than pure Al nanoparticles. Al-Cu nanoparticles have been synthesised using electronic explosion of metal pairs [42] [43] and laser ablation [44]. Al-Mg and Al-Ni alloy nanoparticles have been synthesized using plasma arc evaporation [45]. It is known to electrochemically activate Al, by dissolving the surface oxide layer [46], and thus provides an excellent option for corrosion free Al plasmonics. Additionally, co-precipitation [47] and ball-milling [48] offer other techniques to synthesize Al-alloy nanoparticles.

Recently, A. Malek et al. reported stabilization of Al(0) in water for the first time, using an in-situ reduction process involving copper ions [17]. A thin copper layer formed on the surface of the Al(0) nanoparticles helps prevent the oxidation of Al. Al@Cu core shell nanoparticles of various morphologies including spheres, cubes and cuboids are formed along with some alloy particles. This is of particular interest for aluminum plasmonics, as the presence of the copper helps prevent aluminum oxidation. Cu is itself a well-known plasmonic metal [18], and is likely to improve the plasmonic properties of aluminum. Moreover, cubes are known to have enhanced plasmonic responses, due to their sharp corners [19]. Hence, on paper, Al-Cu nanoparticles may be an attractive option to pursue, however the effect of a Cu shell on the plasmonic properties of the system is unclear.

2.2. Problem Definition and Approach

We define two problems, i.e. two Al-based solutions to noble metal plasmonics:

1. The study of the optical properties of Al-Cu core shell-nanoparticles

On paper, Al-Cu nanoparticles may be an attractive option to pursue, however the effect of a Cu shell on the plasmonic properties of the system is unclear. We therefore undertake a comprehensive computational study of Al@Cu core-shell sphere, cubes and cuboids as well as Al-Cu alloy systems, to investigate the plasmonic utility of these systems.

2. The study of the light trapping ability of Al-alloy nanospheres

In this study, we use the Mie theory, effective medium theories and transfer matrix modelling to carry out studies on the light trapping efficiency in an amorphous thin film solar cell due to plasmonic Al alloy nanoparticles. We study 5 alloy systems, namely: Al-Cu, Al-Au, Al-Ni, Al-In and Al-Mg alloy nanoparticles, and investigate their plasmonic response whilst varying particle sizes and alloy compositions. We calculate

the increase in absorption of the amorphous thin silicon film due to light scattering, and thus demonstrate how Al-alloy nanoparticles can offer a robust alternative to traditional noble metal plasmonics. Although this is a simple approach, and does not consider the total scattering behavior of the NPs (eg. plasmon coupling), our results are in close agreement with more complicated FEM studies carried out on similar systems [49]. Moreover, our method is computationally efficient, does not involve complicated boundary conditions, unlike other methods, and is quick. Therefore, our study is useful for providing a quick analysis of the trends and influence of various factors such as alloy composition. This will be useful in the design of further experiments involving alloyed Al nanoparticles for plasmonic applications.

We demonstrate how these systems may prove to be a viable alternative to existing noble metal plasmonic materials, and also address the environmental corrosion issues of typical Al plasmonics.

CHAPTER 3 : Methods and Techniques

3.1 Al-Cu Core-Shell Nanoparticles

Simulations are carried out using COMSOL Multiphysics 5.4. The scattering and absorption properties of the nanoparticles are studied by solving Maxwell's equations over the nanoparticles using Finite Element Modelling (FEM). This because our study involves cubes and cuboids for which an analytical solution does not exist. Additionally, the results of FEM analysis are in close agreement with that of the Mie Solution (Figure 1b)

3.1.1 Geometry

The nanoparticles, shells, and oxide layers are assumed to be uniform, smooth and symmetric. Spheres are used to model nanospheres, while blocks with rounded corners and edges are used for nanocubes and nanocuboids. The rounding is performed by creating a 2nm fillet along each edge of the block. Core shell nanoparticles are modelled as concentric spheres or blocks. A spherical PML (Perfectly Matched Layer) [50] (Figure 3-1 (b)) of radius $10r_{\text{eff}}$ (where $r_{\text{eff}} = \left(\frac{3}{4\pi V}\right)^{\frac{1}{3}}$, V is the volume of the nanoparticle) is used to truncate calculations in the region. The calculated values are almost constant beyond this PML radius, which is indicative of a convergent solution.

The radius of the particle studies is 100nm. This is because for particles of this size, a scattering peak exists in the visible region (300-800nm), this is not true of 50nm Al nanoparticles (Fig 1(b)). As many of the interesting plasmonic phenomena of nanoparticles are related to its peak scattering and absorption, we felt that a study of 100nm nanoparticles would be a more interesting addition to literature. Moreover, particles with size>100nm will also follow similar trends.

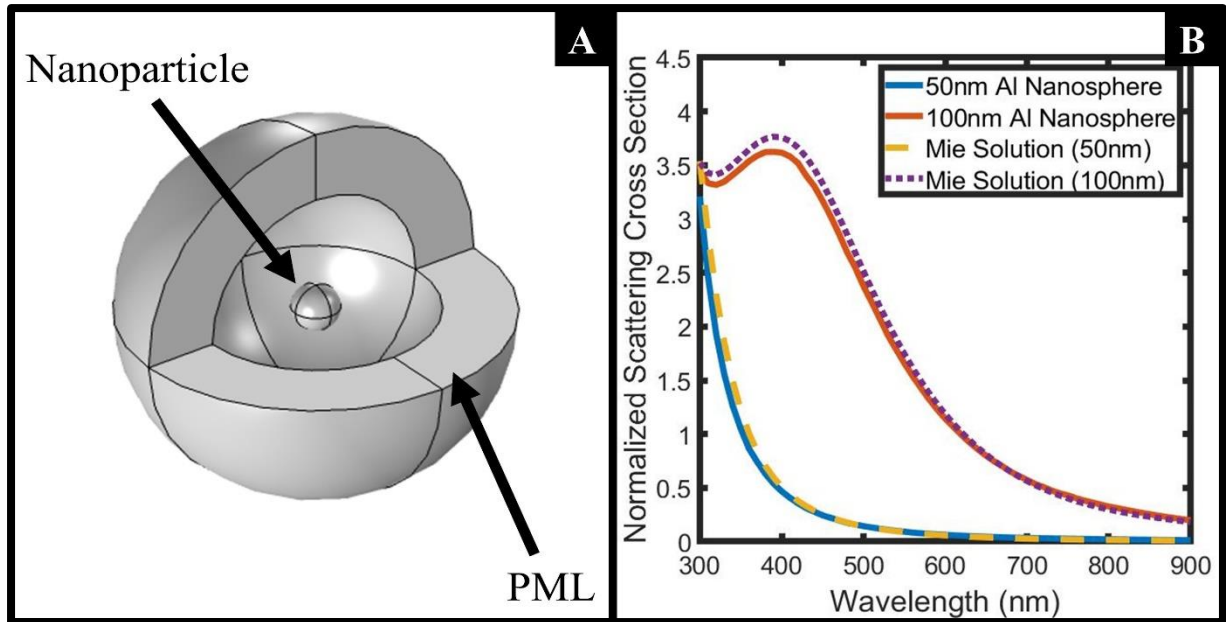


Figure 3-1 (a) Geometry used for simulations. A PML can be used to truncate the computational region to a sphere of radius $\sim 200\text{-}400\text{nm}$. (b) The normalized scattering cross sections of 50nm and 100nm Al nanospheres. A scattering peak exists only for the 100nm nanosphere in the visible region. The Mie Scattering Solutions are in close agreement with the FEM analysis.

3.1.2 Equations

Maxwell's Equation (1) is solved for various input frequencies to obtain the electric field.

$$\nabla \times \frac{(\nabla \times E)}{\mu_r} - k_0^2 \left(\epsilon_r - \frac{j\sigma}{\omega\epsilon_0} \right) E = 0 \quad (1)$$

The incident light is assumed to be along the Z axis. The electric and magnetic fields are resolved along the x and y axis, respectively. The background electric field is taken as a plane wave in the x-direction, and is given as

$$E_x = E_0 e^{-2\pi j nz/\lambda} \quad (2)$$

where n is the refractive index of the surrounding medium.

For an incident energy flux

$$I_{inc} = \frac{nE_0^2}{2Z_0} \hat{k} \quad (3)$$

the scattering cross section for a nanoparticle is defined as:

$$SCS = \frac{\oint I_{sca} \mathbf{n} dS}{I_{inc}} \quad (4)$$

and the absorption cross section is given by:

$$ABS = \frac{\iiint Q_{loss} dV}{I_{inc}} \quad (5)$$

where the integrals are carried out over the nanoparticle surface and volume respectively. The normalized SCS and ABS are obtained by dividing these values by the effective surface area of the nanoparticles in the direction of the incident light.

The simulations are carried out between 300nm and 900nm, as this region corresponds to a large part (about $\sim 43\%$) of the total solar irradiance. The irradiance below 300nm is almost negligible.

3.13 Materials

The complex valued refractive indexes are obtained from the data of Johnson and Christy [51] for gold and copper, Lenham [52] for Al and Dhineshbabu [53] for CuO. The real and imaginary dielectric constants are obtained from this data using the relation

$$\epsilon_r + j\epsilon_i = (n + jk)^2 \quad (6)$$

Since all components are homogenous, for alloys, the mixing rule given by Bergman [54] is applied. For an alloy with mole fraction and relative permittivities of the first component x_1 and ϵ_1 respectively, and that of the second component x_2 and ϵ_2 respectively, the effective permittivity of the alloy is given by:

$$\epsilon_{alloy} = x_1\epsilon_1 + x_2\epsilon_2$$

The surrounding medium is water, with a refractive index of 1.33. The real part of the refractive index is taken to be constant since its variation across the visible spectrum is small (1.349 at 300nm and 1.328 at 900nm). The imaginary part of the refractive index of water is ignored since it is very small (1.02×10^{-9} at 450nm).

3.2 Al-based Alloy Nanoparticles

We have used the Mie Theory, Effective Medium Theory (Bruggeman and Mie-Maxwell Garnett) and Transfer Matrix Modelling to calculate our results. An explanation of each of these methods and the overall methodology used is given below.

2.1 Mie Theory

Mie Theory, developed by Gustav Mie [33], provides a rapid and accurate numerical method for the determination of the optical cross sections of a homogenous sphere in a dielectric medium.

The scattering cross section is a probabilistic measure of how much of the incident light is diverted, or scattered from its path by the sphere. The absorption cross section represents the probability that the incident light is absorbed by the sphere. The extinction cross section is the sum of the absorption and scattering cross sections. Mie calculated an analytic function for the scattering and absorption efficiencies (the cross-sections divided by their geometric cross sections) of a sphere given by:

$$Q_{sca} = \frac{2}{x^2} \sum_{n=1}^{\infty} (2n+1)[a_n^2 + b_n^2] \quad (1)$$

$$Q_{abs} = \frac{2}{x^2} \sum_{n=1}^{\infty} (2n+1)Re[a_n + b_n] \quad (2)$$

$$Q_{ext} = Q_{sca} + Q_{abs} \quad (3)$$

Where $x = \frac{2\pi n_m r}{\lambda}$ is the size parameter (n_m is the refractive index of the surrounding medium, r is the radius of the nanoparticle and λ is the wavelength of the incident light) and a_n and b_n are the calculated Mie coefficients of the scattered field. To calculate these parameters, PyMieScatt [34], an open source Python library was used. The refractive index of the surrounding medium (air) was taken as $1+0i$.

The scattering and absorption ratios, i.e. the proportion of scattering and absorption in the total extinction, are defined as:

$$Q_{abs_ratio} = \frac{Q_{abs}}{Q_{ext}}, \quad Q_{sca_ratio} = \frac{Q_{sca}}{Q_{ext}} \quad (4)$$

To compare the optical properties of nanoparticles across a range of wavelengths, radii, and alloy compositions, all values were weighted with the AM1.5G solar spectrum, values of which were obtained from [35]. For example:

$$Q_{abs_weighted} = \frac{\int_{300}^{900} Q_{abs}(\lambda) AM1.5G(\lambda) d\lambda}{\int_{300}^{900} AM1.5G(\lambda) d\lambda} \quad (5)$$

2.2 Optical Properties of Materials

To calculate the optical properties of metallic nanospheres using the Mie Theory, the parameters needed are the wavelength of incident light (λ), the particle diameter (r) and the complex wavelength dependent refractive indices of the metal, $n(\lambda) + ik(\lambda)$.

The optical constants of were obtained from Rakic [36] for Al, from Johnson [37] for Au, Cu and Ag, from Mathewson for In [38] and from Hagemann [39] for Mg. They are shown graphically in Figure 3-2.

The real and imaginary parts of the relative permittivity of the metals can be obtained from their (n, k) values as:

$$\varepsilon_r = n^2 - k^2, \quad \varepsilon_i = 2ink, \quad \varepsilon = \varepsilon_r + \varepsilon_i \quad (6)$$

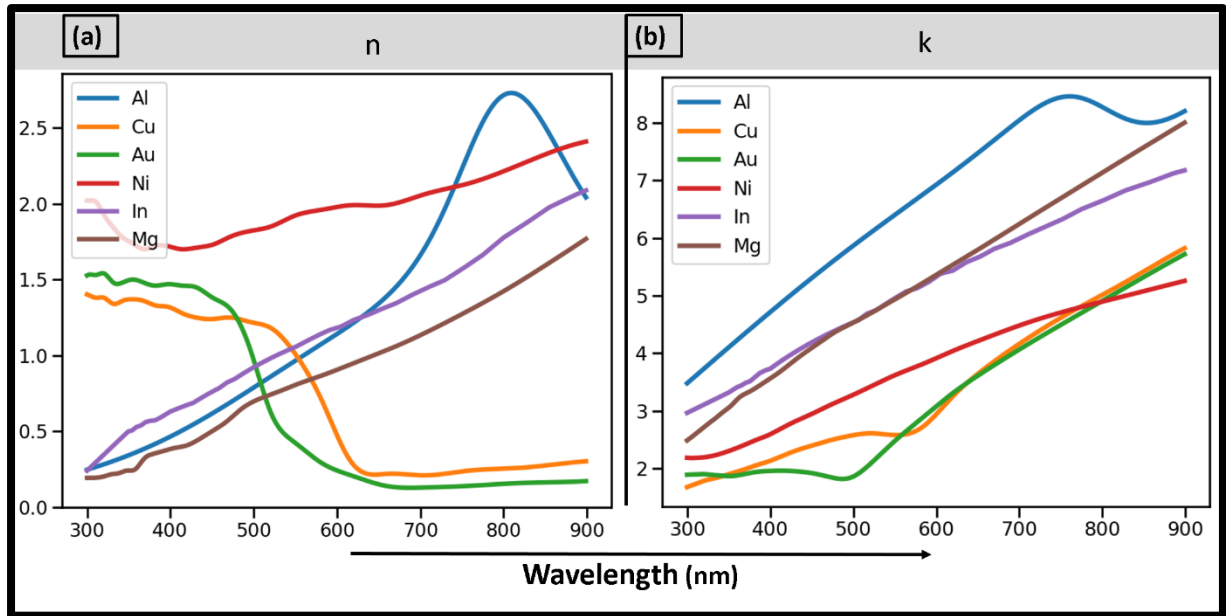


Figure 3-2 (a) n and (b) k values for Cu, Au, Ni, In and Mg in the visible-NIR range (300-900nm). Cu and Au show similar variation in n and k values, as do Mg and In. Therefore, it may be expected that their optical responses are similar.

To compute the optical constants of alloy nanoparticle, the Bruggeman Effective Medium Theory [40] was used. For an alloy with n components, the effective refractive index is given by:

$$\sum_{i=2}^n f_i \frac{(\varepsilon_i - \varepsilon_1)}{(\varepsilon_i + 2\varepsilon_1)} = 0 \quad (7)$$

Where ε_1 is the relative permittivity of the first component, which is Al in our case. ε_i is the permittivity of the other components in the alloy, whilst f_i are their respective volume fractions. The Bruggeman Model assumes that the total flux deviation due to the presence of multiple components is zero. This means that the model is inherently symmetric, and can be used for alloys with a variety of volume fractions of the components.

For an alloy with two components, Al and M, where M=Cu, Au, Ni, In or Mg, as considered in this study, the effective permittivity of the alloy (ε_{eff}) is given as

$$\varepsilon_{eff} = \frac{1}{4} (\beta + \sqrt{\beta^2 + 8\varepsilon_{Al}\varepsilon_M}) \quad (\beta = (3f_{Al} - 1)\varepsilon_{Al} + (3f_M - 1)\varepsilon_M) \quad (8)$$

Where f_{Al} and f_M are the volume fractions of Al and M in the alloy. Notably, when $f_{Al} = 1$, $\varepsilon_{eff} = \varepsilon_{Al}$, as expected. Care must be taken to consider the sign of the square root, depending on the material used.

2.3 Simulation Model

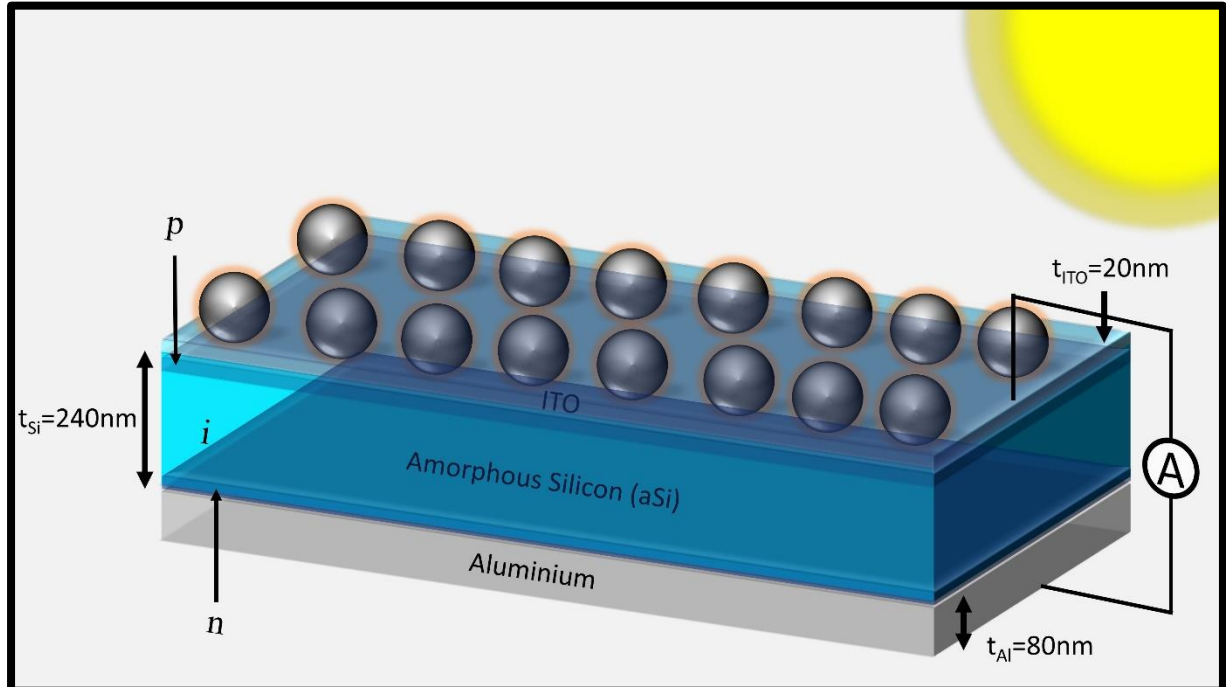


Figure 3-3. The thin film solar cell used for optical simulations. The top and bottom junctions of a:Si (amorphous Silicon) are p and n doped respectively. Since the a:Si layer is so thin, it does not absorb much light. Therefore, plasmonic nanostructures, like the Al-alloy NPs shown here can be added to improve its absorption.

To investigate the utility of plasmonic alloy nanoparticles for enhancing the performance of thin film solar cell, a p-i-n amorphous silicon solar cell was modelled, as shown in Figure 3-3. It consists of an 80nm Al substrate, with 240nm of amorphous hydrogenated Silicon (henceforth designated as a:Si) deposited on it, doped in a p-i-n fashion. Since the doping is small (of the order of ppm), the optical constants of a:Si are assumed not to change with the degree of doping. The optical constants of a:Si and Indium Tin Oxide (ITO) are obtained from [41] and [42] respectively.

We study how the addition of a layer of two-dimensionally arranged Al-alloy plasmonic nanospheres on the surface of the solar cell affects the absorption of the a:Si layer. These calculations are performed using a transfer matrix method (TMM) approach.

2.4 Transfer Matrix Method (TMM)

The Transfer Matrix Method [43] is used to compute the reflection, transmission and absorption of a multi-layered film. As an example, light is incident on a multilayer film which has n layers, beginning with a semi-infinite layer (air) and ending with a semi-infinite substrate. Each layer has its own thickness (T_i) and complex refractive index (RI_i). For example, in our case, as per Table 1:

i	Layer	T_i	RI_i
1	Air	Infinite	1
2	Nanoparticle + Air Layer	$2R_{NP}$	Calculated using Mie-MG Theory
3	ITO	20nm	[41]
4	Amorphous Silicon	240nm	[42]
5	Aluminium	80nm	[36]
6	Air	Infinite	1

Table 1. A list of the layers in the thin film solar cell studied, their thicknesses and refractive indices. The indice i is used in reference to the TMM method.

If the electric field propagating in the i^{th} layer is E_i^+ in the $+x$ direction, and E_i^- in the $-x$ direction, the transmission matrix is given as:

$$M_{ij} = \frac{1}{t_{jk}} \begin{bmatrix} 1 & r_{ij} \\ r_{ij} & 1 \end{bmatrix} \quad (9)$$

Where t_{jk} is the Fresnel Transmission Coefficient and r_{ij} is the Fresnel Reflection Coefficient for interfaces i and j. We define the propagation matrix for a wave in the i^{th} layer as:

$$P_i = \begin{bmatrix} e^{-i(2\pi/\lambda)d_i n_i \cos(\theta_i)} & 0 \\ 0 & e^{i(2\pi/\lambda)d_i n_i \cos(\theta_i)} \end{bmatrix} \quad (10)$$

We then use the local transfer matrix **M:**

$$\begin{bmatrix} E_0^+ \\ E_0^- \end{bmatrix} = M_{01} P_1 M_{12} P_2 \dots \dots M_{s-1} s \begin{bmatrix} E_{substrate}^+ \\ 0 \end{bmatrix} \quad (11)$$

Hence, we can write:

$$\begin{bmatrix} E_0^+ \\ E_0^- \end{bmatrix} = \begin{bmatrix} M_{11} & M_{12} \\ M_{21} & M_{22} \end{bmatrix} \begin{bmatrix} E_{substrate}^+ \\ 0 \end{bmatrix} \quad (12)$$

Then, the reflectance (r) and transmission (t) coefficients become

$$t = \frac{1}{M_{11}}, r = \frac{M_{21}}{M_{11}} \quad (13)$$

Hence, using this approach, the transmission, reflectance and absorbance of each layer in the multilayer stack can be computed. We assume coherent waves, and therefore consider all surfaces to be smooth.

2.5 Mie-Maxwell Garnett Effective Medium Theory

Doyle [44] suggested a modification to the traditional Maxwell Garnett Theory, to evaluate the effective refractive index of a suspension of metallic spheres. His approach, is given as:

$$\frac{\epsilon_{eff} - \epsilon_{medium}}{\epsilon_{eff} + 2\epsilon_{medium}} = f_v \frac{3i}{2x^3} a_{1(Al-M)} \quad (14)$$

Where ϵ_{eff} the effective permittivity of the alloy, ϵ_{medium} is the permittivity of the surrounding medium, x is the size parameter defined earlier, $a_{1(Al-M)}$ is the first Mie coefficient for an Al-M alloy with size parameter x . f_v is the volume fraction of metal spheres in the suspension. f_v is related to the surface coverage (F) as $f_v = \frac{2}{3}F$. Since this model only considers the polarizability of the inclusions: i.e. the suspension of spheres, it fails for large volume fractions. Since the Mie-MG Theory is restricted to $f_v < 0.5$. we consider f_v values between 0.1 and 0.4.

For our study, we consider Air + NPs as a distinct nanocomposite layer, and use the Mie-MG Theory to calculate its effective refractive index. The problem is then reduced to that of a multilayer stack, layers starting with air, followed by the air-NP nanocomposite, then ITO, a:Si and finally Al. Using the Transfer Matrix Method, we calculate the percentage of incident light absorbed of the a:Si layer as a function of incident wavelength, surface coverage(F), alloy composition (f_{Al}) and R_{NP} .

In most cases, we plot the enhancement, and increase (Δ) in the absorption of a:Si due to the presence of Al-alloy NPs, relative to the absorption of bare a:Si, defined as:

$$Enhancement = \frac{\int_{300}^{900} p_{Si_with_NP}(\lambda) AM1.5G(\lambda) d\lambda}{\int_{300}^{900} p_{Si_bare} AM1.5G(\lambda) d\lambda}, \quad (15)$$

$$\Delta = \frac{\int_{300}^{900} (p_{Si_with_NP} - p_{Si_bare})(\lambda) AM1.5G(\lambda) d\lambda}{\int_{300}^{900} p_{Si_bare} AM1.5G(\lambda) d\lambda} \quad (16)$$

Python code was written to implement the Mie Theory, Bruggeman and Mie-MG Effective Medium Theory and the Transfer Matrix Modelling. The results of our model closely match the FEM analysis of a similar system carried out by Akimov et al. [35]. A summary of our method is provided in Figure 3-4.

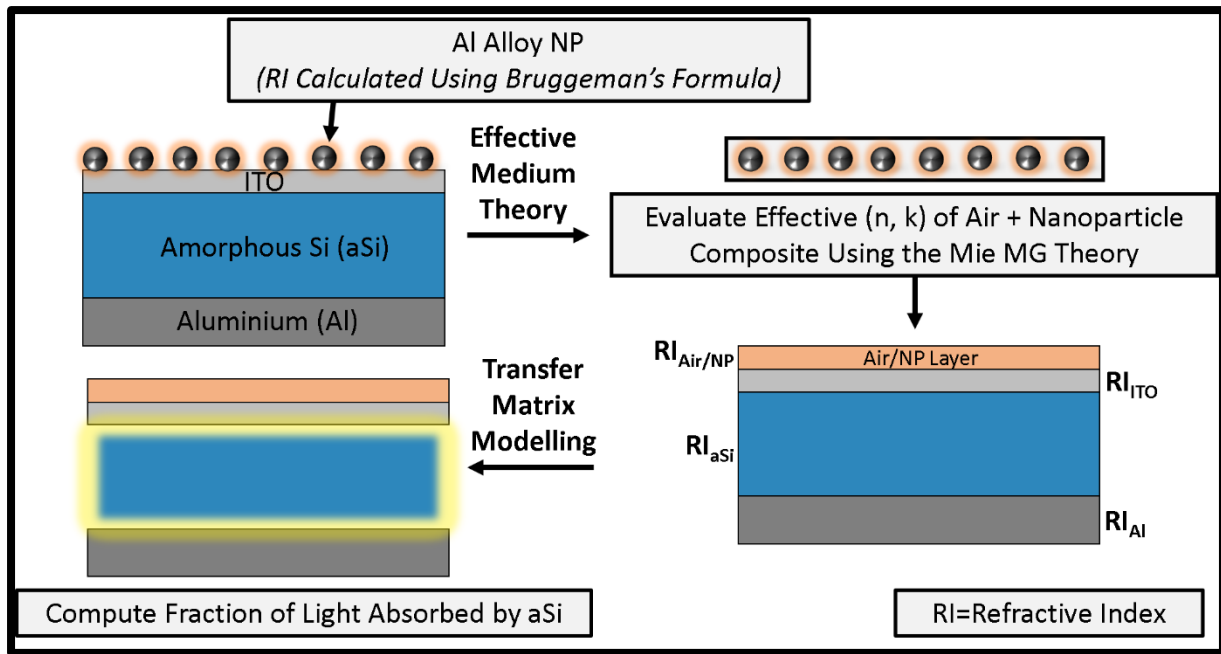


Figure 3-4. A summary of the methods used for the calculation of the optical parameters of alloy nanoparticles, and their effect on the absorption by a substrate. Since all the methods used are numerical, the technique is computationally efficient.

CHAPTER 4 : Results and Discussion: Al-Cu Core-Shell Applications

Recently, A. Malek et al. reported stabilization of Al(0) in water for the first time, using an in-situ reduction process involving copper ions [47]. A thin copper layer formed on the surface of the Al(0) nanoparticles helps prevent the oxidation of Al. Al@Cu core shell nanoparticles of various morphologies including spheres, cubes and cuboids are formed along with some alloy particles. This is of particular interest for aluminum plasmonics, as the presence of the copper helps prevent aluminum oxidation. Cu is itself a well-known plasmonic metal [48], and is likely to improve the plasmonic properties of aluminum. Moreover, cubes are known to have enhanced plasmonic responses, due to their sharp corners [49]. Hence, on paper, Al-Cu nanoparticles may be an attractive option to pursue, however the effect of a Cu shell on the plasmonic properties of the system is unclear. We therefore undertake a comprehensive computational study of Al@Cu core-shell sphere, cubes and cuboids as well as Al-Cu alloy systems, to investigate the plasmonic utility of these systems.

4.1 Al-Cu Core Shell Nanoparticles

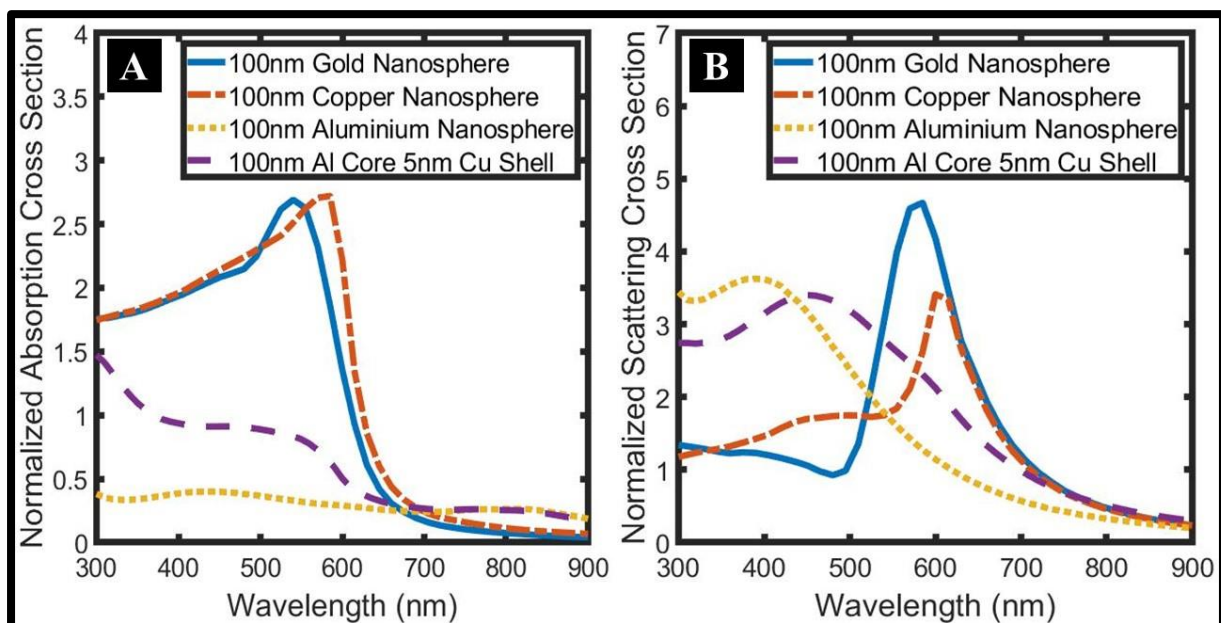


Figure 4-1 Normalized (a) absorption and (b) scattering cross sections of 100nm Au, Cu, Al and Al-Cu core-shell nanospheres. Al@Cu is a better absorber of light than Al, but worse than

Au and Cu. Both Al and Al@Cu show higher scattering cross sections than Au and Cu between 300nm and 500nm.

Simulations are carried out on 100nm gold, copper, aluminum and a 100nm Al sphere with a 5nm Cu shell. Figure 4-1 shows that Al@Cu nanospheres absorb almost twice as much light than Al between 300 and 550nm, but not as well as Au or Cu nanospheres. Both Al and Al@Cu are better scatterers of light than Au and Cu in the 300-500nm region. It can also be seen that the scattering peak of Al@Cu is redshifted from 390nm to 450nm when compared to Al nanospheres. This opens the possibility of engineering the peak positions by varying core-shell ratios.

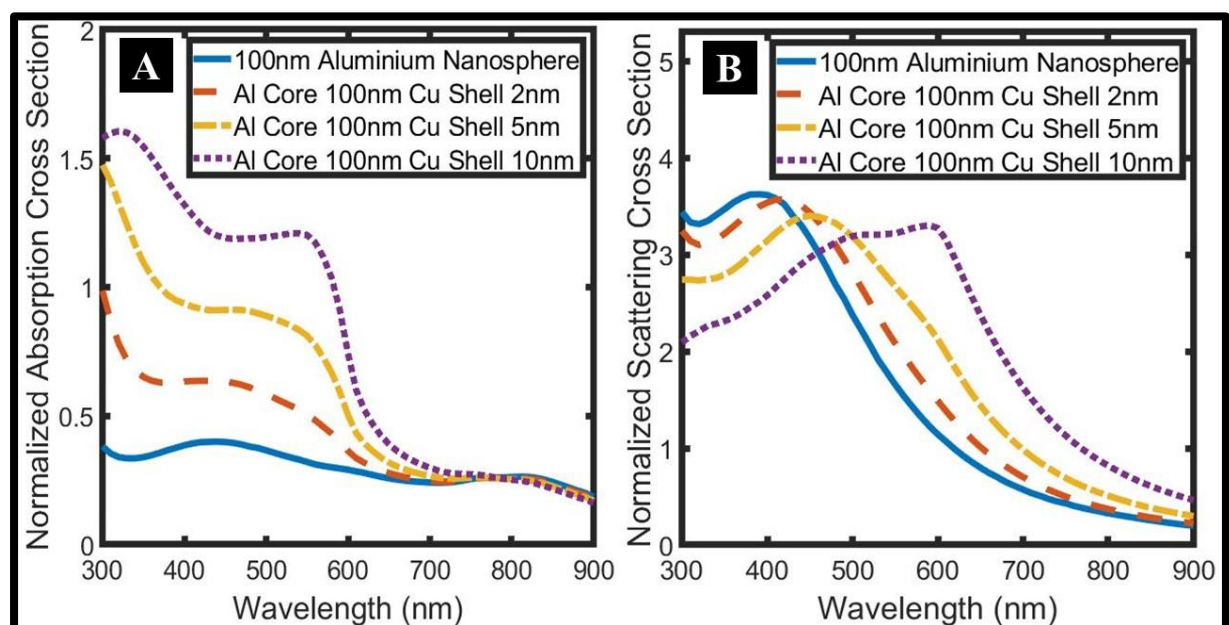


Figure 4-2. Effect of shell thickness on the normalized (a) absorption and (b) scattering cross-sections of 100nm nanospheres. The absorption cross sections monotonically increase with shell thickness. A 10nm shell shifts the scattering peak from 390 to 590nm while slightly decreasing the peak scattering intensity from 3.64 to 3.3

The normalized absorption cross sections of these nanospheres increases as the thickness of the copper shell increases (Fig Figure 4-2a). For example, their values at 500nm for 100nm Al cores with 2nm, 5nm and 10nm Cu shells are 0.36, 0.58, 0.89 and 1.19 respectively. A thicker Cu shell also redshifts the peak scattering intensity (Fig Figure 4-2b). Calculations performed over the core and shell for a 100nm Al nanosphere with a 5nm Cu shell at 500nm reveal that

the shell contributes to 64.4% of the absorption cross section, with the remaining contribution coming from the core. At the same wavelength, when the shell thickness is increased to 10nm, the contribution of the shell increases to 81.4%. Two peaks are seen in the scattering curve, as the Cu shell thickness is increased, the second peak (the one at a higher wavelength) becomes more pronounced. We define the peak intensity as that of the peak with the highest intensity.

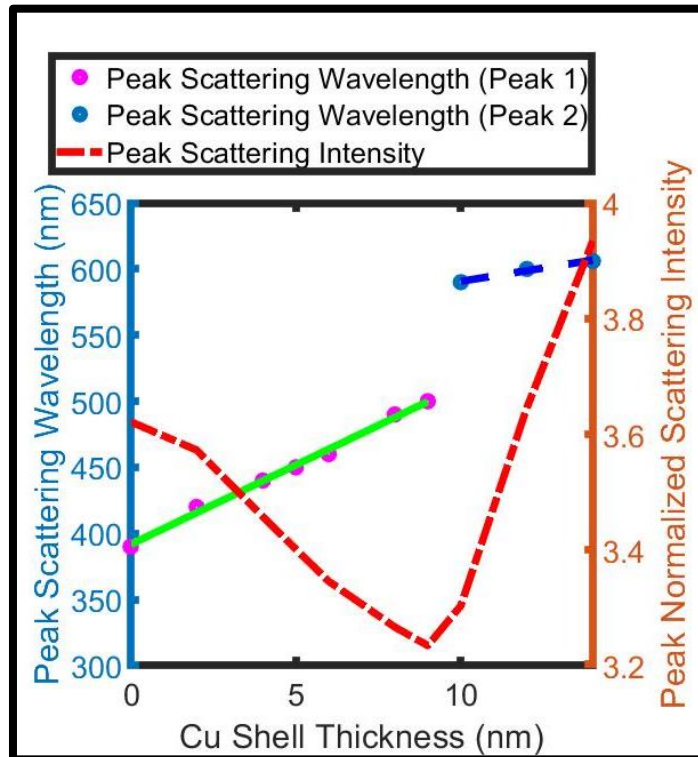


Figure 4-3 Variation of peak normalized scattering intensity and wavelength of a 100nm Al nanosphere with Cu shell thickness. The peak wavelength follows the equation $\lambda_{max} = 391.7 + 12t$ for t between 0 and 9nm and $\lambda_{max} = 550.7 + 4t$ for t between 10nm and 14nm, where t is the thickness of the shell

Figure 4-3 shows that a 10nm Cu shell can shift the peak scattering intensity from 390nm to 590nm, as the second peak becomes more prominent. The corresponding normalized peak scattering intensity does not show a substantial decrease, going from 3.64 to 3.3, a decrease of about 9%. This is of vital importance for light harvesting applications as the region from 400-700nm encompasses ~ 43% of the total solar irradiance. We have provided a design equation which may be used to engineer the peak scattering wavelengths by varying the shell thickness between 0 and 12nm (Figure 4-3).

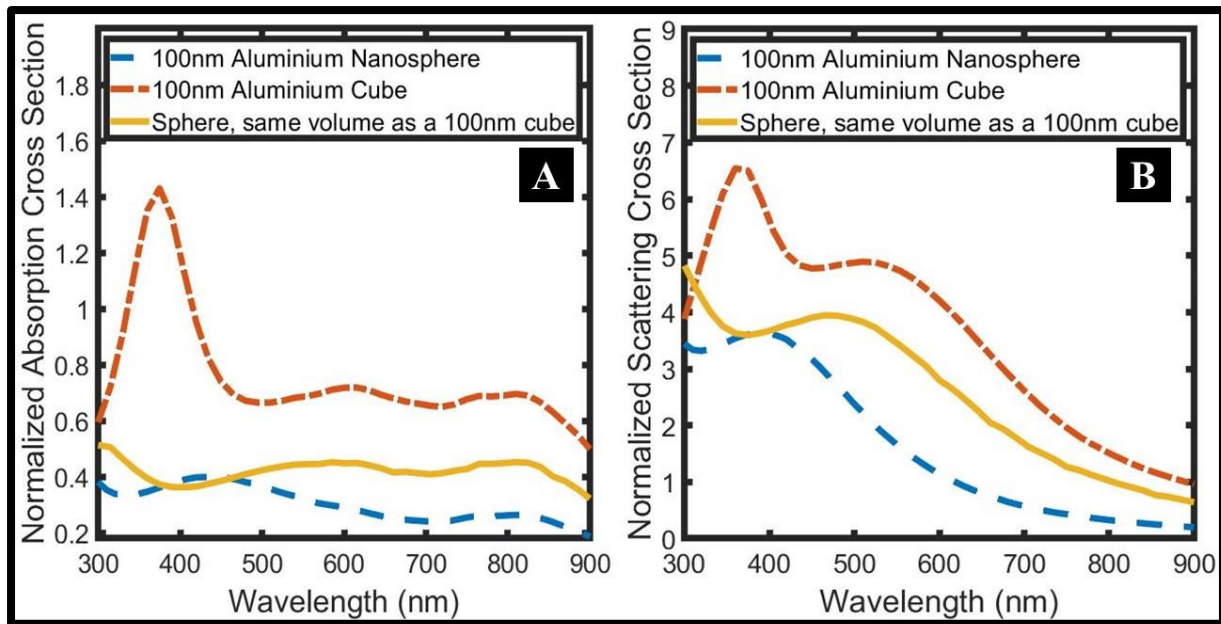


Figure 4-4 Comparison of normalized (a) absorption and (b) scattering coefficients of a 100nm Al nanosphere, a 100nm Al cube, and a sphere with the same volume as the cube. Absorption and scattering peaks are seen between 300 and 400nm for a cube, with a 250% and 175% improvement in ABS and SCS respectively w.r.t a sphere at these peaks.

A comparison between cubical and spherical nanoparticle morphologies reveals that a cubical nanoparticle exhibits higher scattering and absorption power than a sphere of the same volume Figure 4-4. This implies that for the same mass of metal, a cubic geometry is preferred. This is because the polarization charge redistributes over the larger surface area of the cube, resulting in a higher SCS and ABS. Recent reports have shown that Al nanocubes have sharp corners [19]. A cube also shows redshifted absorption and scattering peaks when compared to a sphere. When charges accumulate at a sharp area like the corner of a nanocube, there is a separation between the electron cloud and the positive core. Thus the restoring columbic force is diminished, and the increased separation leads to red shifting of the absorption and scattering bands [67]. Al-Cu core-shell nanocubes could therefore offer an opportunity for further enhancement of the optical properties of aluminum, and its tenability.

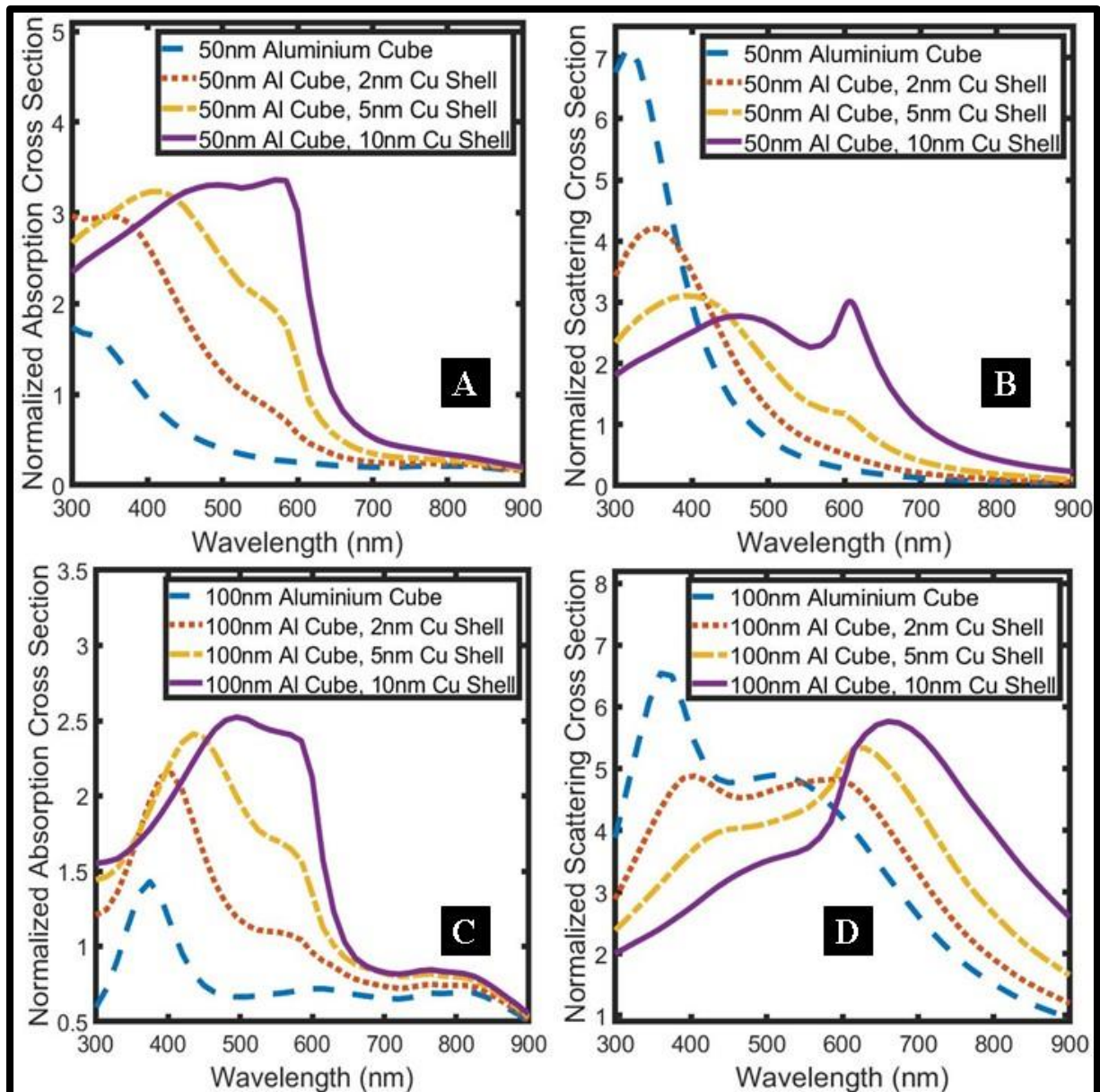


Figure 4-5 Effect of shell thickness on the normalized absorption and scattering cross-sections of (a) & (b) 50nm and (c) & (d) 100nm nanocubes. The absorption peak shifts from 375nm to 480nm and the scattering peak shifts from 360nm to 660nm when the shell thickness is changed from 0 to 10nm.

Calculations of the effect of Cu shell thickness on the optical properties of Al nanocubes are carried out (Figure 4-5). Two peaks are seen in the scattering curve. As the Cu shell thickness is increased, the second peak (the one at a higher wavelength) becomes more pronounced. The effect of shell thickness on the absorption and scattering peaks is summarized in Fig. 6. Calculations performed over the core and shell for a 100nm Al nanocube with a 5nm Cu shell at 500nm reveal that the shell contributes to 70% of the absorption cross section, with the

remaining contribution coming from the core. At the same wavelength, when the shell thickness is increased to 10nm, the contribution of the shell increases to 84.3%.

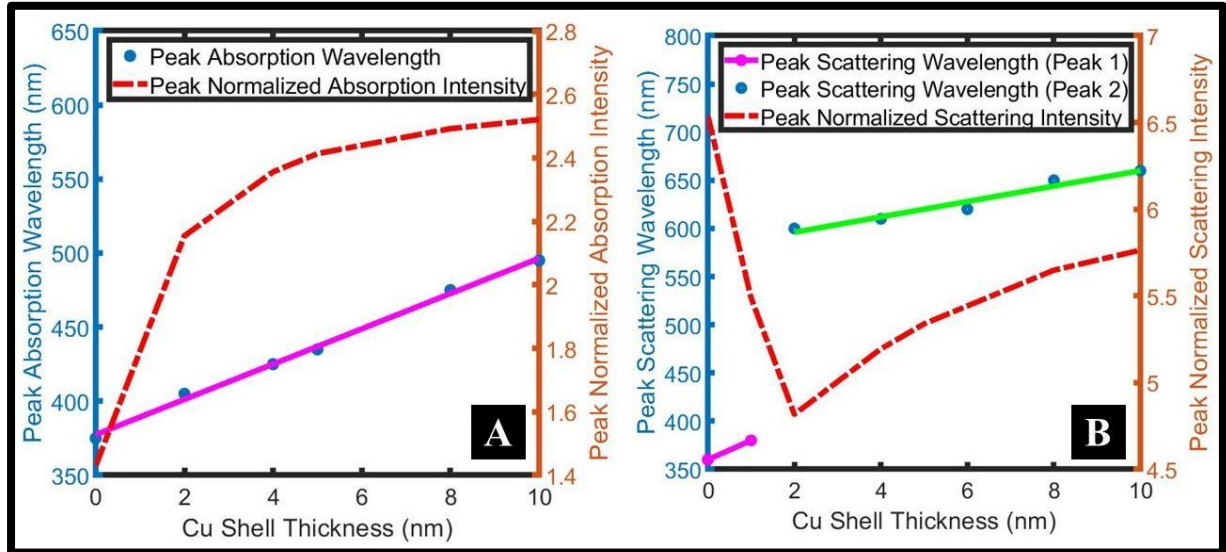


Figure 4-6 Variation of normalized (a) absorption and (b) scattering intensities and wavelengths of 100nm Al cubes with Cu shell thickness. The normalized absorption peak follows the equation $\lambda_{ABS_{max}} = 377.4 + 11.91t$ and the normalized scattering peak (the peak with the highest magnitude) follows the equation $\lambda_{SCS_{max}} = 580 + 8.0t$, where t is the thickness of the Cu shell varying between 2nm and 10nm.

A linear increase in peak absorption wavelength with increasing shell thickness is shown in Figure 4-6(a). The peak absorption wavelength shifts linearly from 375nm to 480nm with the addition of a 10nm Cu shell. The corresponding peak absorption intensity increases too, going from a normalized value of 1.4 to 2.56, an increase of 86%.

Since two distinct peaks are seen in the scattering cross sections, we define the scattering peak here as the one with a higher magnitude, as in the case of spheres. The scattering peak shifts from 360nm to 660nm when a 10nm Cu shell is added, as the second peak becomes more prominent (Fig. Figure 4-6b). While a standalone Al cube exhibits a peak normalized scattering intensity of 6.5, this value decreases to 4.87 when a 2nm shell is added, and increases to 5.75 when the shell thickness is increased to 10nm. This is a decrease of about 11.5% from a 100nm Al nanocube with no shell. Thus, a Cu shell can be used to shift the peak scattering intensity

of Al nanocubes to the visible region (660nm) with only a small decrease in peak scattering intensity. The design equation which may be used to engineer the wavelength of the peak absorbance and the primary scattering peak by varying the shell thickness between 2 and 10nm is shown to be linear (Figure 4-6).

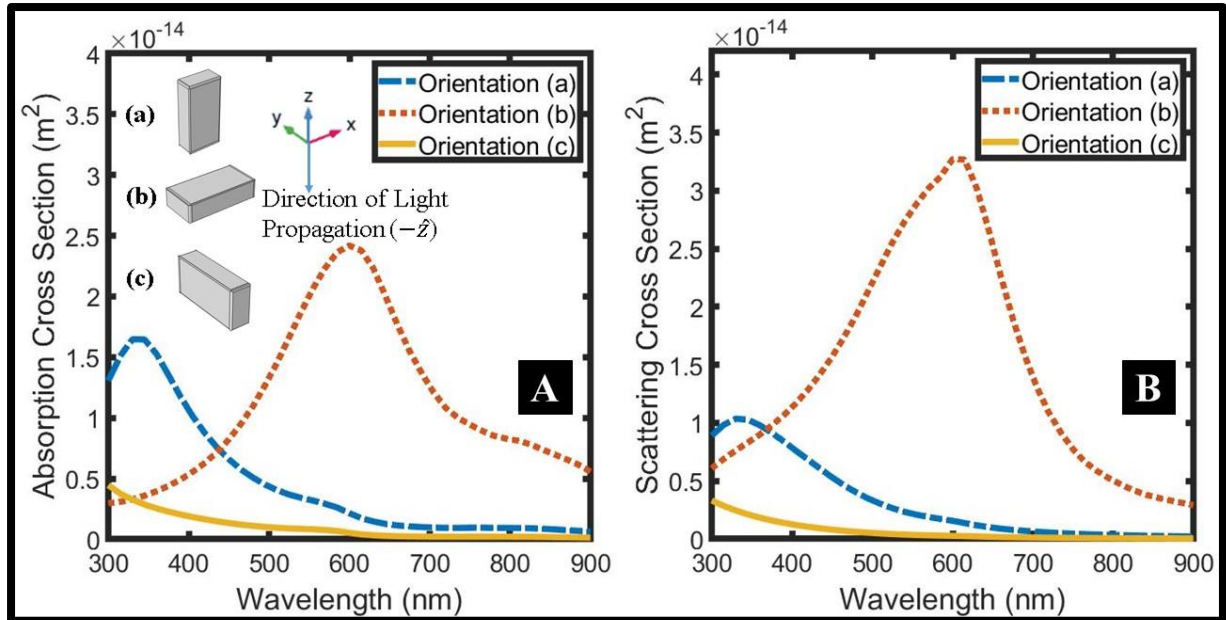


Figure 4-7 Variation of (a) absorption and (b) scattering cross sections of three different orientations w.r.t. the xy plane for a nanocuboid with dimensions 50nm, 25nm and 100nm coated with a 2nm Cu shell. Orientation (b) covers a large part of the solar spectrum between 400 and 700nm.

For nanocuboids, a degree of asymmetry is introduced, hence the orientation of the cuboid becomes important. Figure 4-7 shows the variation in absorption and scattering intensities for three different orientations of the nanocuboid in the x-y plane. Unsurprisingly, orientation (b) shows higher absorption and scattering cross sections as it has the maximum surface area in the direction of incident light. Orientation (a) shows both absorption and scattering peaks at 330nm, while orientation (b) shows these peaks at 600nm. Thus, depending on the orientation of the nanocuboid, the UV (200nm-360nm) or visible (400nm-700nm) of the solar spectrum may be harnessed. A mixture of these orientations may enable light harvesting over the entire solar spectrum.

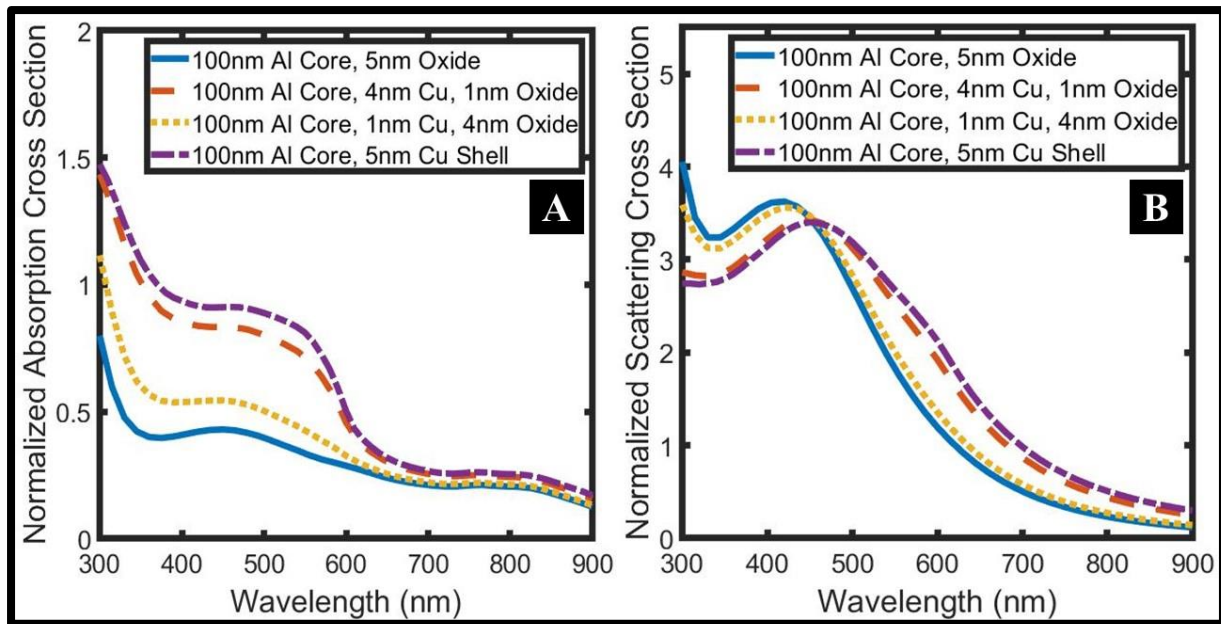


Figure 4-8 Effect of oxide thickness on the normalized (a) absorption and (b) scattering cross section of Al-Cu core-shell nanospheres. A 1nm oxide layer does not produce a perceptible effect on the absorption or scattering curves.

Copper, if used in air or an oxygenated medium, is susceptible to oxidation. To investigate the effect of oxidation we assumed that a copper shell is consumed by a uniform CuO layer of varying thicknesses. For very thin shells $\sim 5\text{nm}$, the native oxide thickness is below 1nm [68] for room temperature oxidation. For 1 nm oxide shell, the effect on normalized absorption and scattering cross sections is remarkably low (Fig. Figure 4-8), with the curves for a 5nm Cu shell, and a 4nm Cu shell covered by a 1nm oxide layer almost indistinguishable.

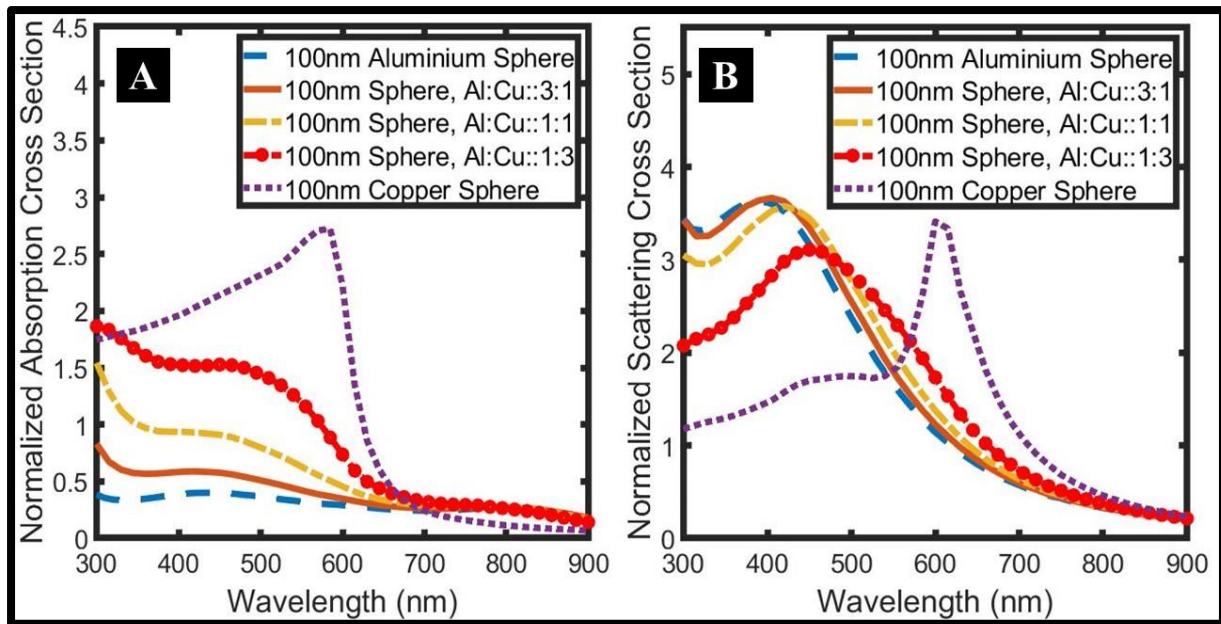


Figure 4-9 Effect of alloy composition on the (a) absorption and (b) scattering cross sections of 100nm spherical Al-Cu alloys. Increasing Cu content increases the absorption cross section, while a compositional invariance is observed in scattering cross sections for Cu content up to 50%.

One way to alleviate the effects of surface oxidation is by alloying. Cu and Al form a solid solution which covers a large part of their phase diagram. As expected, increasing the proportion of copper increases the absorption cross section of alloyed nanospheres (Figure 4-9). We expect the scattering cross sections to increase with increasing Al content. However, the scattering curves for an Al alloy with 0%, 25% and 50% copper are remarkably similar. This is similar to the compositional invariance in scattering cross sections reported in Al-In alloys [69].

Finally, we investigate the absorption and scattering cross sections of a variety of dimeric arrangements of spheres and cubes of equal volume (as shown in Figure 4-10). The general trend seen is that a dimer of two spheres is better for increasing the scattering cross-sections, while a dimer of two cubes (at an angle of 45 degrees with each other) results in the best absorption cross sections. Figure 4-11 shows the associated electric fields for the configurations in Figure 11.

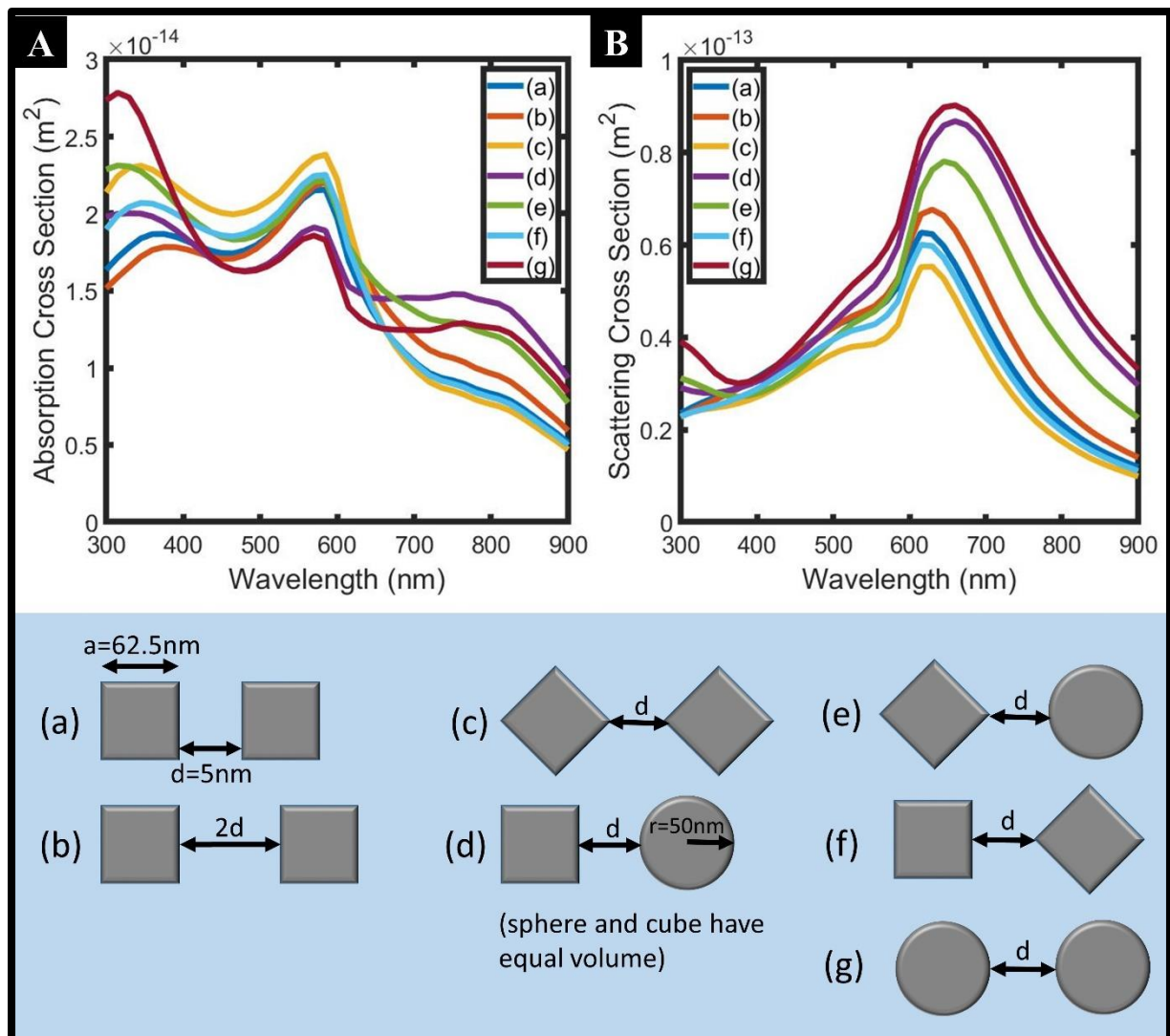


Figure 4-10 (a) Absorption and (b) Scattering cross sections of a variety of dimeric arrangements of a nanocube and nanosphere (both of the same volume). A dimer of two cubes at an angle of 45 degrees with each other (orientation (c)) shows the lowest scattering cross sections ($5.5 \times 10^{-14} \text{ m}^2$) at peak scattering wavelength but the highest absorption cross section ($5.5 \times 10^{-14} \text{ m}^2$) in the 400-800nm range.

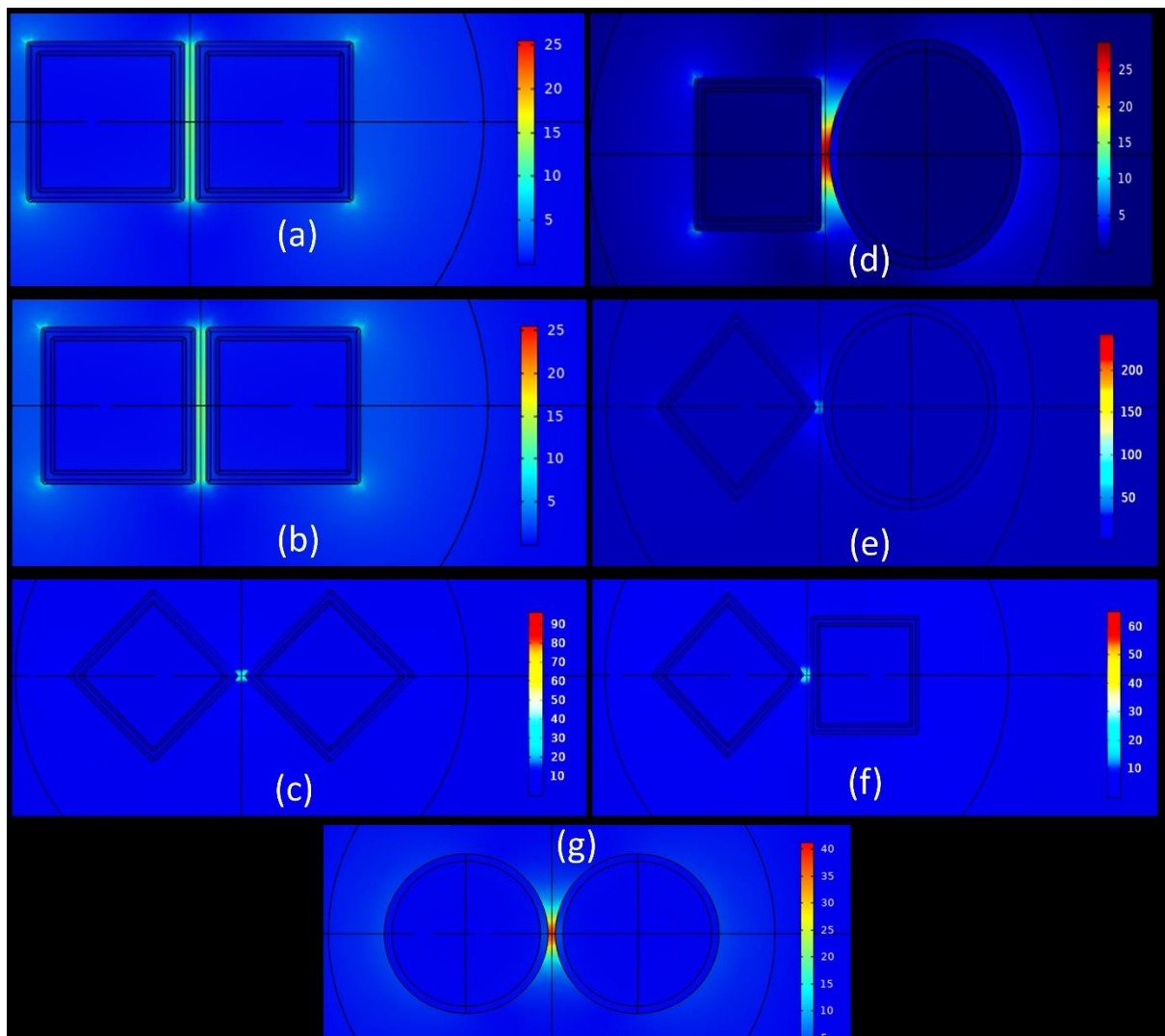


Figure 4-11 Associated electric fields for configurations (a) to (f) corresponding to Figure 11 at a wavelength of 670nm.

CHAPTER 5 : Results and Discussion: Al-M Alloy Nanoparticles

In this study, we use the Mie theory, effective medium theories and transfer matrix modelling to carry out studies on the light trapping efficiency in an amorphous thin film solar cell due to plasmonic Al alloy nanoparticles. We study 5 alloy systems, namely: Al-Cu, Al-Au, Al-Ni, Al-In and Al-Mg alloy nanoparticles, and investigate their plasmonic response whilst varying particle sizes and alloy compositions. We calculate the increase in absorption of the amorphous thin silicon film due to light scattering, and thus demonstrate how Al-alloy nanoparticles can offer a robust alternative to traditional noble metal plasmonics. Although this is a simple approach, and does not consider the total scattering behaviour of the NPs (eg. plasmon coupling), our results are in close agreement with more complicated FEM studies carried out on similar systems [49]. Moreover, our method is computationally efficient, does not involve complicated boundary conditions, unlike other methods, and is quick. Therefore, our study is useful for providing a quick analysis of the trends and influence of various factors such as alloy composition. This will be useful in the design of further experiments involving alloyed Al nanoparticles for plasmonic applications.

5.1.1 Al-alloy nanoparticles

Simulations were performed on Al-Cu, Al-Au, Al-Ni, Al-In and Al-Mg alloys nanospheres with radii varying between 1 and 100nm, and alloy composition (f_{Al} is the volume fraction of Al) varying between 0 and 1. Their optical constants are calculated using the Bruggeman Formula detailed above, and all results were weighted with the AM1.5G solar spectrum to allow for easier comparison.

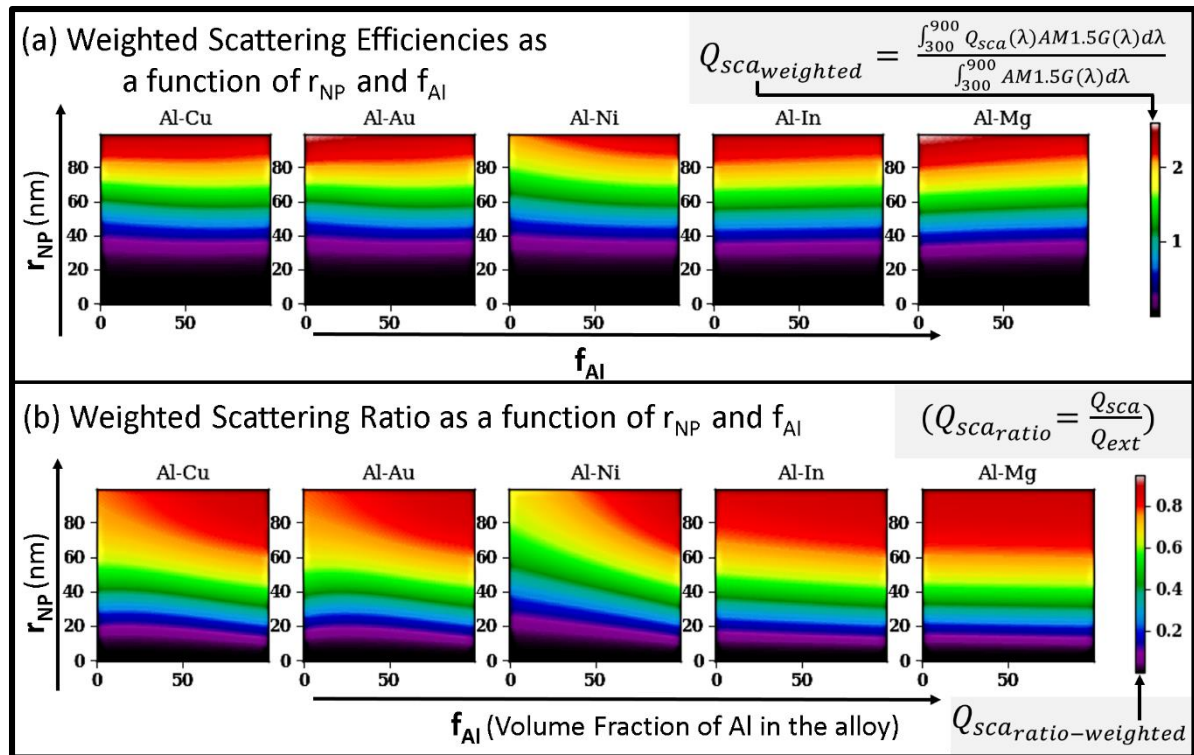


Figure 5-1 Weighted (a) scattering efficiencies and (b) scattering ratios for Al alloyed with five different metals, as a function of their radii and volume fraction of Al. $Q_{sca_ratio_weighted}$ is 0.76 for a 50% ($f_{Al}=0.5$) Al-Mg alloy of radius 60nm ($R_{NP}=60nm$), as opposed to 0.74, 0.63, 0.71 and 0.7 for Al-In, Al-Ni, Al-Au and Al-Cu NPs respectively, with the same composition and radius. Thus, Al-In and Al-Mg display the best scattering behavior at a given f_{Al} and R_{NP} .

Figure 5-1 shows the weighted scattering efficiencies and scattering ratios for the alloy compositions chosen. Al-Cu and Al-Au NPs show similar scattering behaviour: this is unsurprising as their optical constants are quite similar in the wavelength range studied, as mentioned earlier. The scattering efficiency and scattering ratio increases with increasing nanoparticle radius (R_{NP}), for a fixed alloy composition. While the scattering efficiencies decrease with increasing volume fraction of Al (f_{Al}) for a given radius in the case of Al-Cu, Al-Au and Al-Ni, they increase in the case of Al-In and Al-Mg. Therefore, for a given nanoparticle radius (R_{NP}) with volume fraction of Al= f_{Al} , Al alloyed with In and Mg offers the best scattering performance. For example, for NPs with volume fraction of Al=50% ($f_{Al}=50\%$) and $R_{NP}=60nm$ $Q_{sca_weighted}$ is 1.3, 1.3, 1.21, 1.33 and 1.35 for Al-Cu, Al-Au, Al-Ni, Al-In and Al-Mg

respectively.

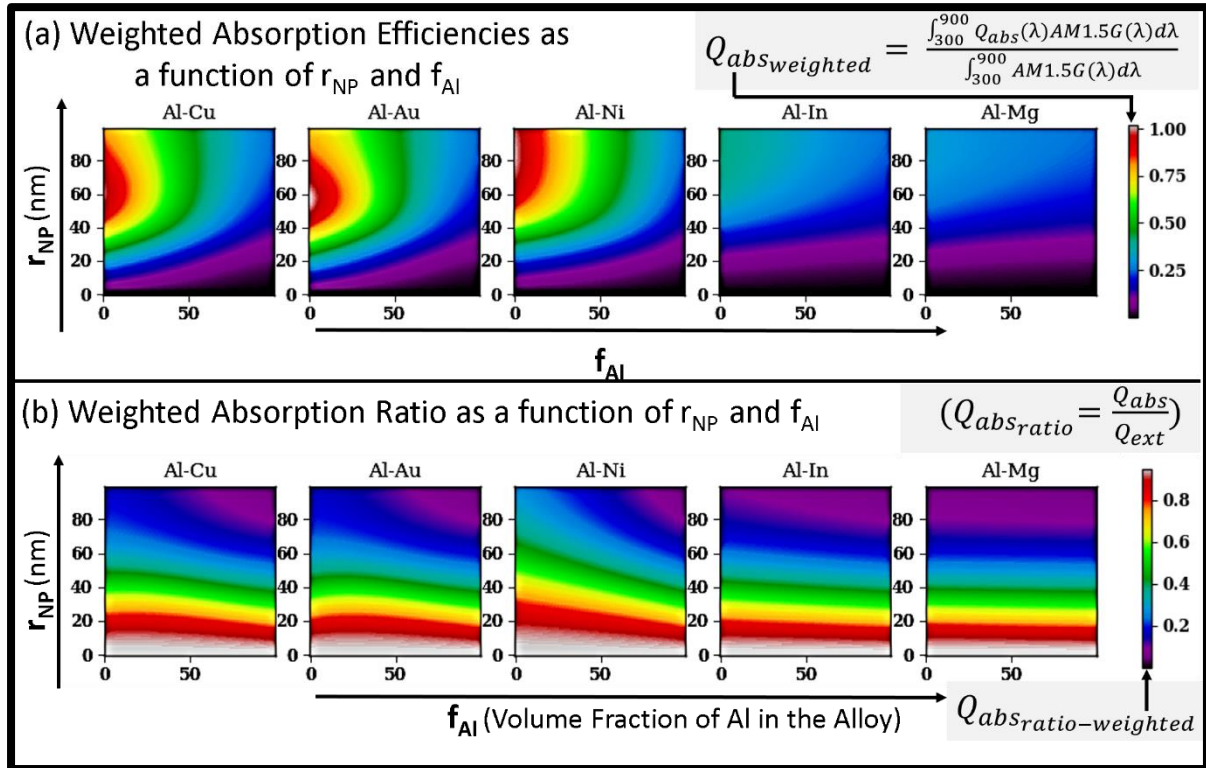


Figure 5-2. Weighted (a) absorption efficiencies and (b) absorption ratios for Al alloyed with five different metals, as a function of their radii and volume fraction. $Q_{abs_ratio_weighted}$ is 0.894 for a 50% Al-Ni alloy of radius 20nm, as opposed to 0.79, 0.77, 0.85 and 0.86 for Al-In, Al-Mg, Al-Au and Al-Cu NPs respectively, with the same composition and radius. Thus, Al, Al-Au, Al-Cu and Al-Ni display the best absorption behavior at a given f_{Al} and R_{NP} .

Figure 5-2 shows the absorption efficiencies and absorption ratios of the nanoparticles studied in Figure 5-1. Figure 5-2b shows that for small particle sizes, up to $R_{NP}=25$ nm, absorption dominates the total extinction. For a fixed composition, an increase in radius results in an increase in absorption efficiency but a decrease in absorption ratio. This means, that as R_{NP} increases, although the contribution of scattering to the overall extinction decreases, the absorption efficiency increases. Figure 5-2a shows that, for a fixed R_{NP} and volume fraction of Al (f_{Al}), Al-Cu, Al-Au and Al-Ni nanoparticles are better absorbers than Al-In and Al-Mg. For example, for NPs with $f_{Al}=50\%$ and $R_{NP}=20$ nm, $Q_{abs_weighted}$ is 0.19, 0.14, 0.15, 0.06 and 0.06 for Al-Cu, Al-Au, Al-Ni, Al-In and Al-Mg respectively. Additionally, for a fixed R_{NP} , increasing f_{Al} results in a decrease in $Q_{abs_weighted}$.

For plasmonic solar cells, the nanoparticles should exhibit low parasitic absorption and high scattering efficiency. However, it can be seen that on increasing R_{NP} , the scattering and absorption efficiencies both increase, even though the absorption ratio decreases. Therefore, an optimum radius, there has to be subtle interplay between Q_{sca} and the parasitic absorption Q_{abs} . However, on increasing f_{Al} , the scattering efficiency increases whilst the absorption efficiency decreases, therefore prospective Al-alloy based NPs for plasmonic solar cell applications should have a high Al content. Hence, Al rich alloy nanoparticles of Al-In and Al-Mg appear to show promise for thin film solar cell applications.

The reason for this lies in the fact that Al has the highest n and k values in the visible spectrum. In and Mg exhibit n and k values closest to Al, whilst the corresponding values for Au, Cu and Ni are further away. Therefore, alloying Al with In and Mg produces plasmonic behaviour similar to pure Al, whilst there are significant disparities observed with Al-Au, Al-Ni and Al-Cu alloy nanoparticles.

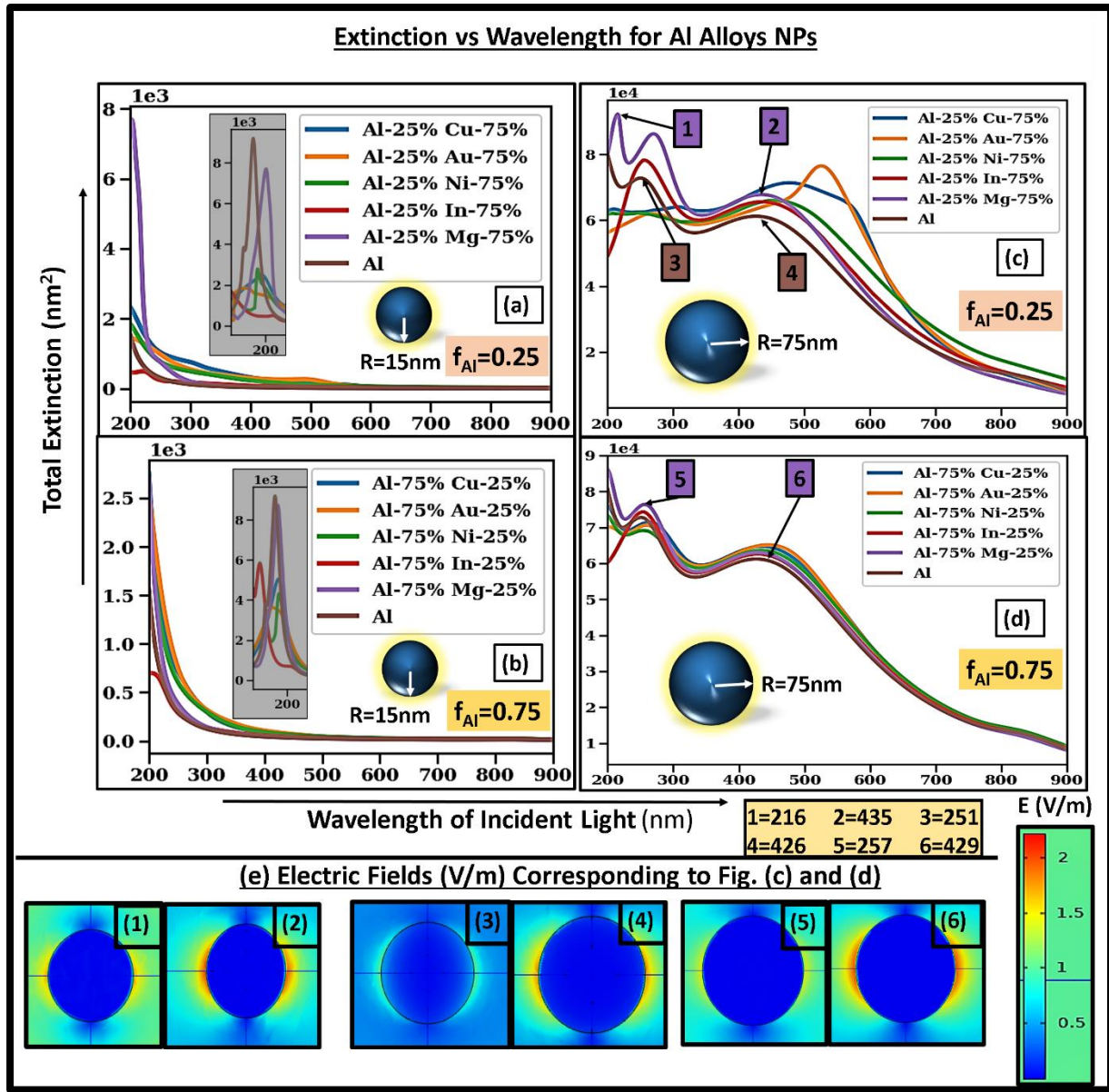


Figure 5-3. Extinction as a function of wavelength for different nanoparticle sizes and alloy compositions. For $R_{NP}=15\text{nm}$, the resonant wavelengths lie in the 100-200nm range, as shown in the inset figures (a) and (b). For larger nanoparticles ($R_{NP}=75\text{nm}$), as seen in (c) and (d), the resonant peaks exist in the visible-NIR (300-900nm) region, and multipolar contributions to the extinction can be seen e.g. Al-Mg ($f_{\text{Al}}=75\%$) in (c). The electric fields corresponding to the marked resonant wavelengths in (b) and (d) are shown in (e). For Al-rich alloys ((b) and (d)), the extinction curves converge, which means that they will show a similar optical response.

Figure 5-3 shows the extinction as a function of wavelength for Al-alloy nanoparticles at two radii, $R_{NP}=15\text{nm}$ and $R_{NP}=75\text{nm}$, and two alloy volume fractions, $f_{\text{Al}}=25\%$ (denoted as Al-25% M-75%) and $f_{\text{Al}}=75\%$ (denoted as Al-75% M-25%). Figure 5-3(c) and Figure 5-3(d) show that if the alloy is Al rich, the extinction curves of all the 5 alloys, namely Al-Cu, Al-Au, Al-Ni,

Al-In and Al-Mg converge, which means that they will show a similar optical response. This is crucial for the design of plasmonic Al-alloy nanoparticles, as it offers great design flexibility for the alloying metal.

3.2 Plasmonic Enhancement of Absorption of Amorphous Silicon in a Thin Film Solar Cell Using Al-alloy NPs

We now use the Mie-MG and TMM method to determine the absorption of the amorphous silicon layer when the Al alloy nanoparticles studied in the subsection above are used to enhance light trapping. The term ‘bare Si’ is used to refer to the arrangement shown in Figure 3-3, but without the layer of nanoparticles.

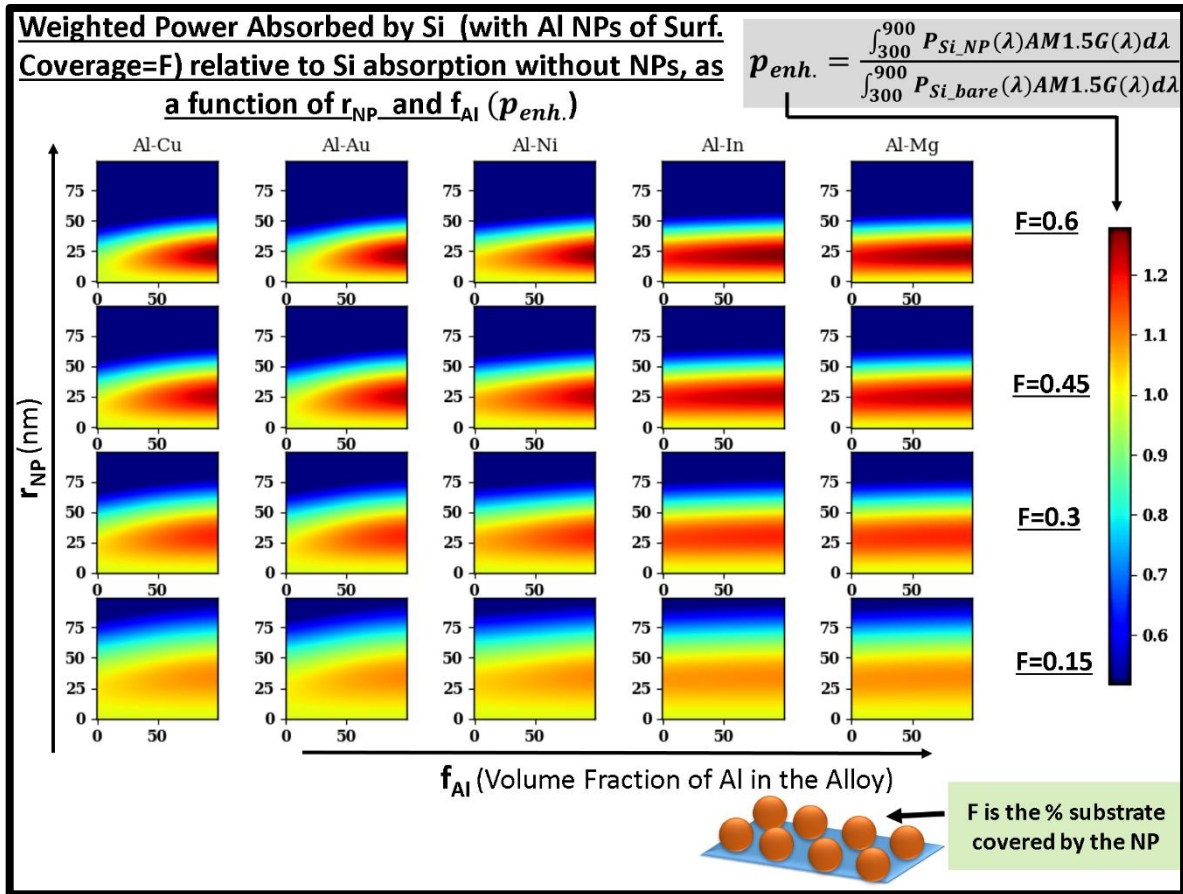


Figure 5-4. The power absorbed by a:Si, weighted by the AM1.5G solar spectrum, relative to the power absorbed by a:Si. Al-In and Al-Mg alloys The maximum absorption enhancement of the a:Si layer increases with increasing surface coverage (1.04 for Al-Mg when $F=0.15$ to 1.28 for Al-Mg when $F=0.6$) However the wavelength at which the maximum occurs decreases with increasing F . Al-In and Al-Mg show a high (>20%) absorption enhancement for a:Si for a wide alloy composition.

Figure 5-4. shows the variation in the absorption enhancement, i.e. the ratio between absorption of a:Si with the alloy-NPs, to a Si without NPs, in the 300-900nm regime, weighted by the AM1.5G solar spectrum. The peak enhancement (1.28 or 28%) occurs for Al-In and Al-Mg alloys. It can be seen that the peak enhancement increases with increasing surface coverage (F) of the nanoparticles, however, the radius at which the peak enhancement F occurs decreases. This will be further discussed later on.

Additionally, it can be seen that the largest enhancement in a:Si absorption occurs for Al-rich alloys, especially in the case of Al-Cu, Al-Au and Al-Ni, while there is some compositional flexibility in the case of Al-In and Al-Mg. For example, when $F=0.6$ and $R_{NP}=20\text{nm}$, if $f_{Al}=0.25$, the enhancement due to the NPs is 3%, 1%, 8%, 21% and 23% for Al-Cu, Al-Au, Al-Ni, Al-In and Al-Mg respectively. For the same radius and F , if $f_{Al}=0.75\text{m}$ the enhancement due to the NPs is 23%, 23%, 23%, 28% and 28% for Al-Cu, Al-Au, Al-Ni, Al-In and Al-Mg respectively. Therefore, Al-In and Al-Mg alloys appear to show the best light trapping behaviour for a wide range of alloy compositions. This is perhaps, due to the similarity in the optical constants of Al, In and Mg in the (300-900nm) range.

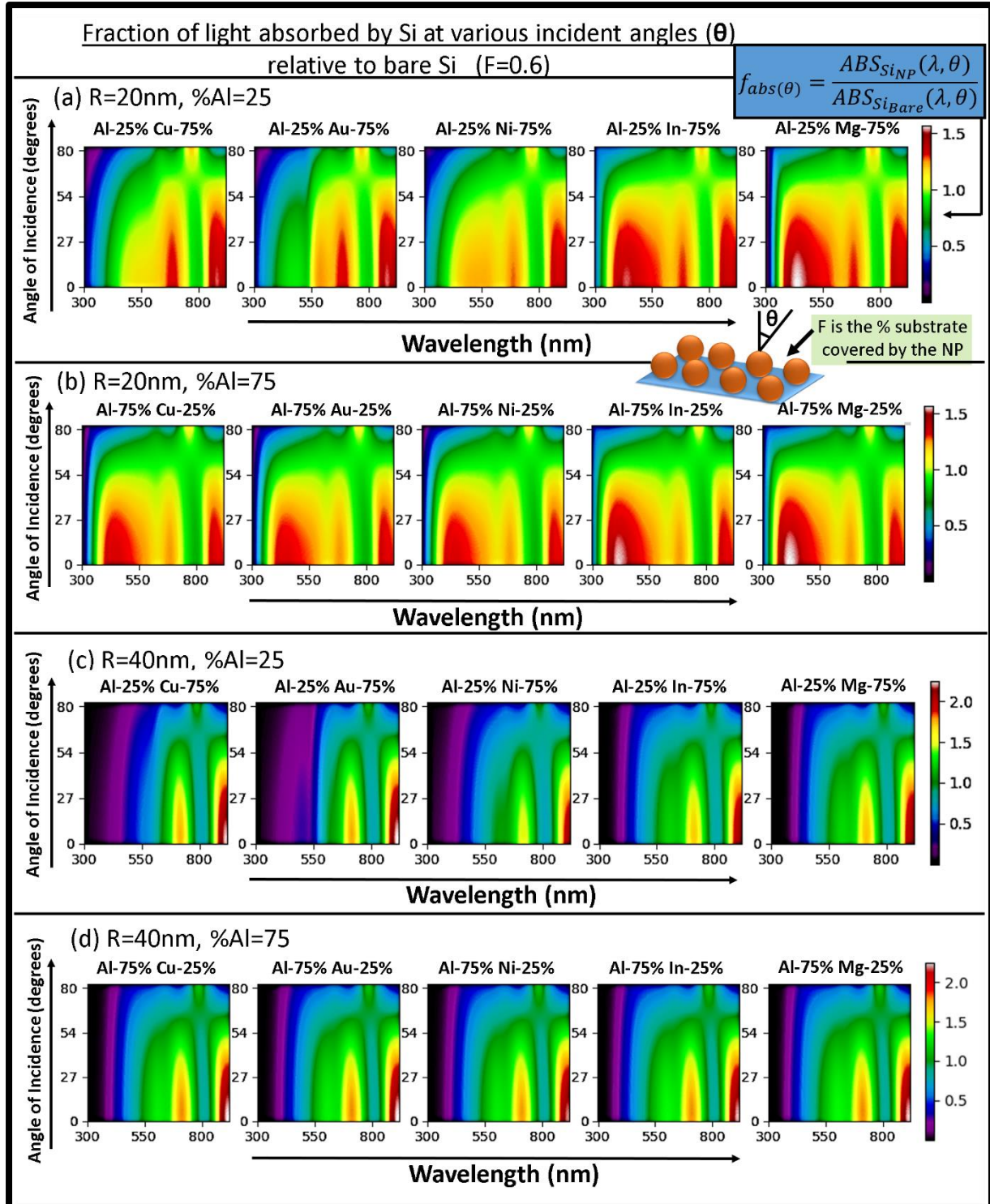


Figure 5-5. The fraction of light absorbed by a:Si with varying incident angles of incident light, relative to the light absorbed by bare Si, for a fixed surface coverage ($F=0.6$) for different values of R_{NP} and f_{AI} . (b) shows that when $f_{AI}=75\%$, the NPs show better angular absorption than in (a) where $f_{AI}=25\%$ for AOI between 0 and 54 degrees. (a) and (b) ($R_{NP}=20\text{nm}$) show a wider range of enhancement (>1) than (c) and (d) ($R_{NP}=40\text{nm}$).

We now look at the effect of the angle of incidence (AOI) on the plasmonic enhancement of absorption of a:Si. We fix $F=0.6$, and study the effect of the AOI on a:Si absorption for two

radii, $R_{NP}=20\text{nm}$, and $R_{NP}=40\text{nm}$, for two alloy compositions, $f_{Al}=25\%$ and $f_{Al}=75\%$. Our results are shown in Figure 5-5, where we plot the enhancement, i.e. the power absorbed by a:Si with NPs divided by the power absorbed by bare a:Si (at the same value of AOI and the wavelength). When $R_{NP}=20\text{nm}$, as in Figure 5-5(a) and Figure 5-5(b), the enhancement is above 1 for a large wavelength regime (400-900nm) and a large angular spread (0-54 degrees). However, when $R_{NP}=40\text{nm}$, as in Figure 5-5(c) and Figure 5-5(d), the enhancement is above 1 only for a wavelength regime between (575-900nm).

Additionally, when $f_{Al}=75\%$, an increased enhancement in absorption of a:Si is seen, especially in the (400-550nm) regime for AOI between 0 and 27degrees, for all the alloys studied. For example, consider the values of the absorption of a:Si at $AOI=20$ degrees and a wavelength of 400nm. When $f_{Al}=25\%$, the enhancement is -5%, -14%, 11%, 41% and 45% for Al-Cu, Al-Au, Al-Ni, Al-In and Al-Mg respectively. For the same AOI and wavelength when $f_{Al}=75\%$, the enhancement is 41%, 39%, 40%, 47% and 48% for Al-Cu, Al-Au, Al-Ni, Al-In and Al-Mg respectively. Hence, Al-rich alloys offer better angular scattering behaviour too, for an AOI between 0 and 54 degrees.

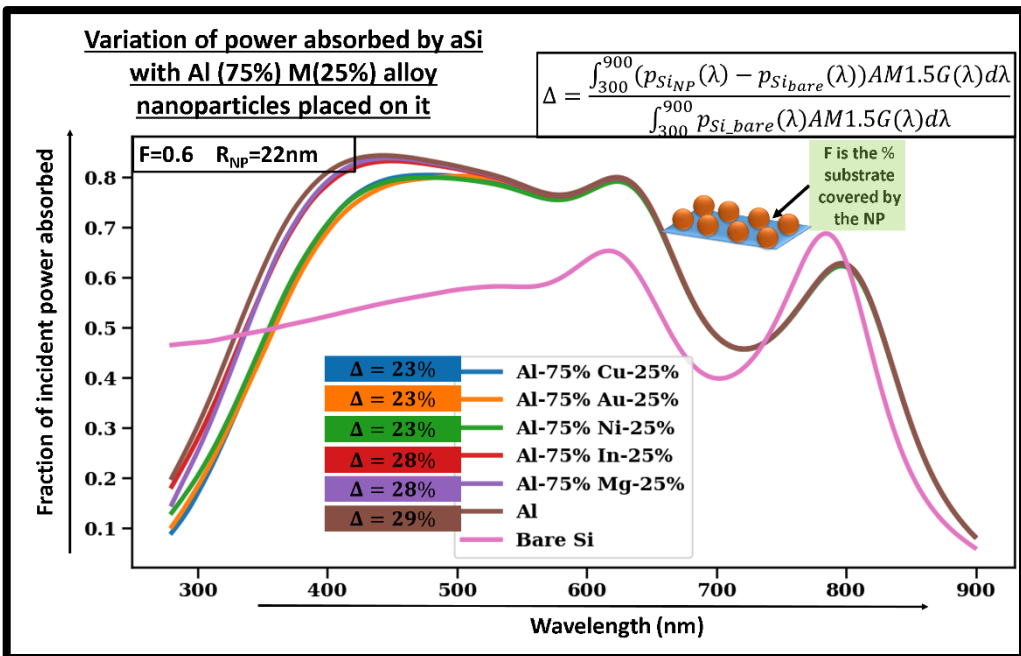


Figure 5-6. The fraction of incident power absorbed by a:Si vs wavelength for Al (75%)-M (25%) alloys. Al, (Al-75% Mg-25%) and (Al-75% In-25%) improve the absorption of a:Si to the maximum extent (29%, 28% and 28% respectively). Thus, a small amount of alloying of Al NPs with these metals does not affect their light trapping efficiency much.

To further investigate the effect of Al-rich NPs, we show the variation between the fraction of incident power and the wavelength in Figure 5-6. The Al-rich alloy nanoparticles considered are of the form (Al-75% M-25%), in terms of respective volume fractions (f_{Al}), also denoted as Al-75% M-25%. The surface coverage F is 0.6, while the radius of the nanoparticles is 22nm. We use the enhancement Δ as defined before. (Al-75% Cu-25%), (Al-75% Au-25%), (Al-75% Ni-25%), (Al-75% In-25%) and (Al-75% Mg-25%) show a Δ of 23%, 23%, 23%, 28% and 28% respectively. The enhancement for pure Al NPs is 29%. Thus, Al-In and Al-Mg alloys show the highest enhancement in the absorption of a:Si, of the systems considered. Also, this shows that a small amount of alloying (25%) can be used to provide corrosion resistance to the Al NP whilst not having a detrimental effect on the plasmonic light trapping.

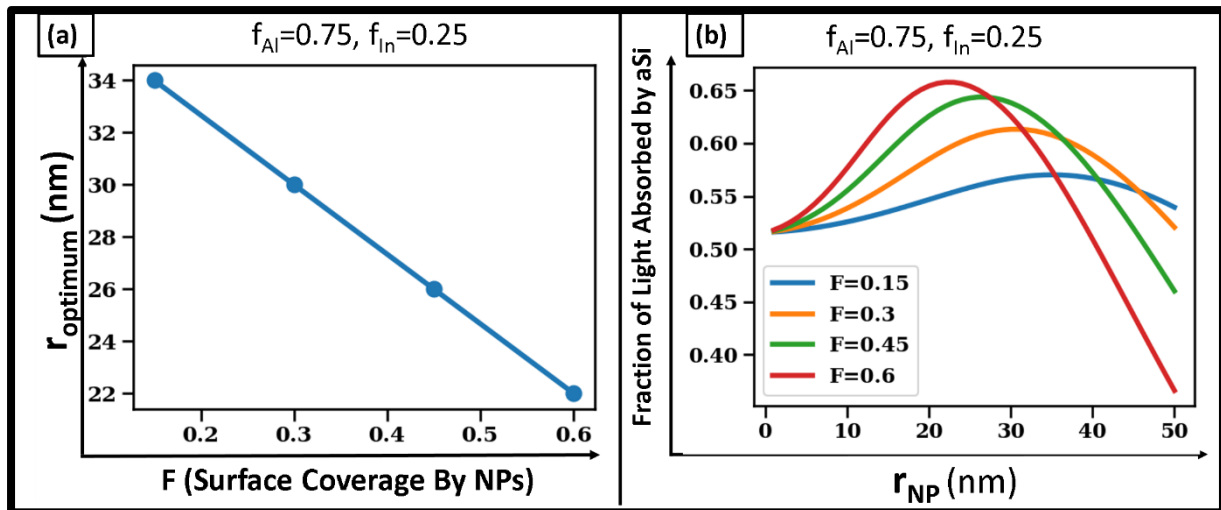


Figure 5-7. (a) The variation between the surface coverage (F) and the optimum radius for an alloy with 75% Al and 25% In. A decreasing linear relation is seen: as F increases, R_{NP} decreases linearly. (b) The variation between the fraction of incident light absorbed by a:Si and the R_{NP} for the same alloy described in part (a). The graph clearly shows that there is a “optimum” radius for each F for maximum light absorption.

We now focus our discussion on a specific alloy with $f_{Al}=75\%$ and $f_{In}=25\%$, also denoted as (Al-75% In-25%). The relationships between the surface coverage (F) and the radius of the alloy nanoparticles, R_{NP} is shown in Figure 5-7. Figure 5-7(a) shows the variation of the optimum radius: $R_{optimum}$ (i.e. the radius at which a:Si absorbs the maximum fraction of incident light) as a function of F . A linear decrease is seen. When $F=0.6$, $R_{optimum}$ is 22nm, however when $F=0.15$, $R_{optimum}$ increases to 34nm. This may be understood as: as F increases, the parasitic absorption increases. A decrease in the optimum value of R_{NP} helps offset this loss.

Figure 5-7(b) shows that for every value of F , there exists a optimum value of R_{NP} for which optimum absorption by a:Si occurs. As R_{NP} increases, the fraction of light absorbed by a:Si increases, reaches a maximum value, and then decreases. Additionally, as seen in Figure 5-5, when $F=0.6$, better angular scattering was shown by $f_{Al}=0.75$ and $R_{NP}=20$ nm, which is close to the value of $R_{optimum}$ (22nm) for $F=0.6$.

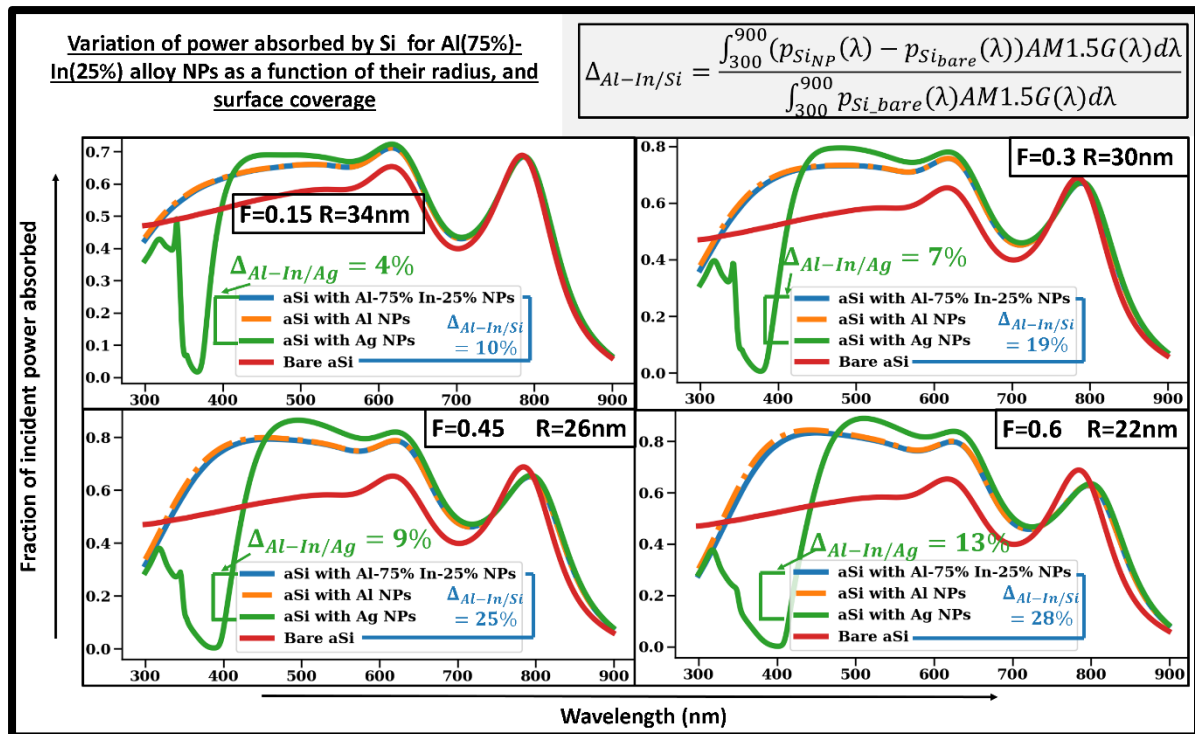


Figure 5-8. The absorption of a:Si as a function of wavelength for different surface coverages for an Al alloy with 75% In.. For each value of F , the radius of the NPs were taken as $R_{optimum}$, which was calculated earlier. The improvement due to the presence of the Al-In NPs is marked in the figure. When $F=0.6$, the presence of Al-In NPs of size 22nm results in a 28% increase in a:Si absorption relative to a:Si without NPs, and a 13% increase in a:Si absorption relative to a:Si with Ag NPs of the same radius placed on it.

Figure 5-8. shows the absorption of a:Si as a function of wavelength for different values of the surface coverage (F), when different NPs with radii corresponding to the $R_{optimum}$ of F are placed on it. When $F=0.6$, the presence of Al-In NPs of size 22nm results in a 28% increase in a:Si absorption relative to a:Si without NPs. Hence, we see that the enhancement due to the presence of Al-In NPs increases with increasing F . Additionally, the absorption curves with Al-In NPs are very similar to that of Al NPs, suggesting that a small amount of In can be added to stabilize Al, without affecting its optical response. Moreover, Al-In alloy NPs show a better enhancement in the absorption of a:Si than Ag NPs of the same size when weighted across the 300-900nm region. When $F=0.6$, Al-In NPs on a:Si show a 112% increase in a:Si absorption relative to a:Si with Ag NPs of the same radius (28% vs 13%).

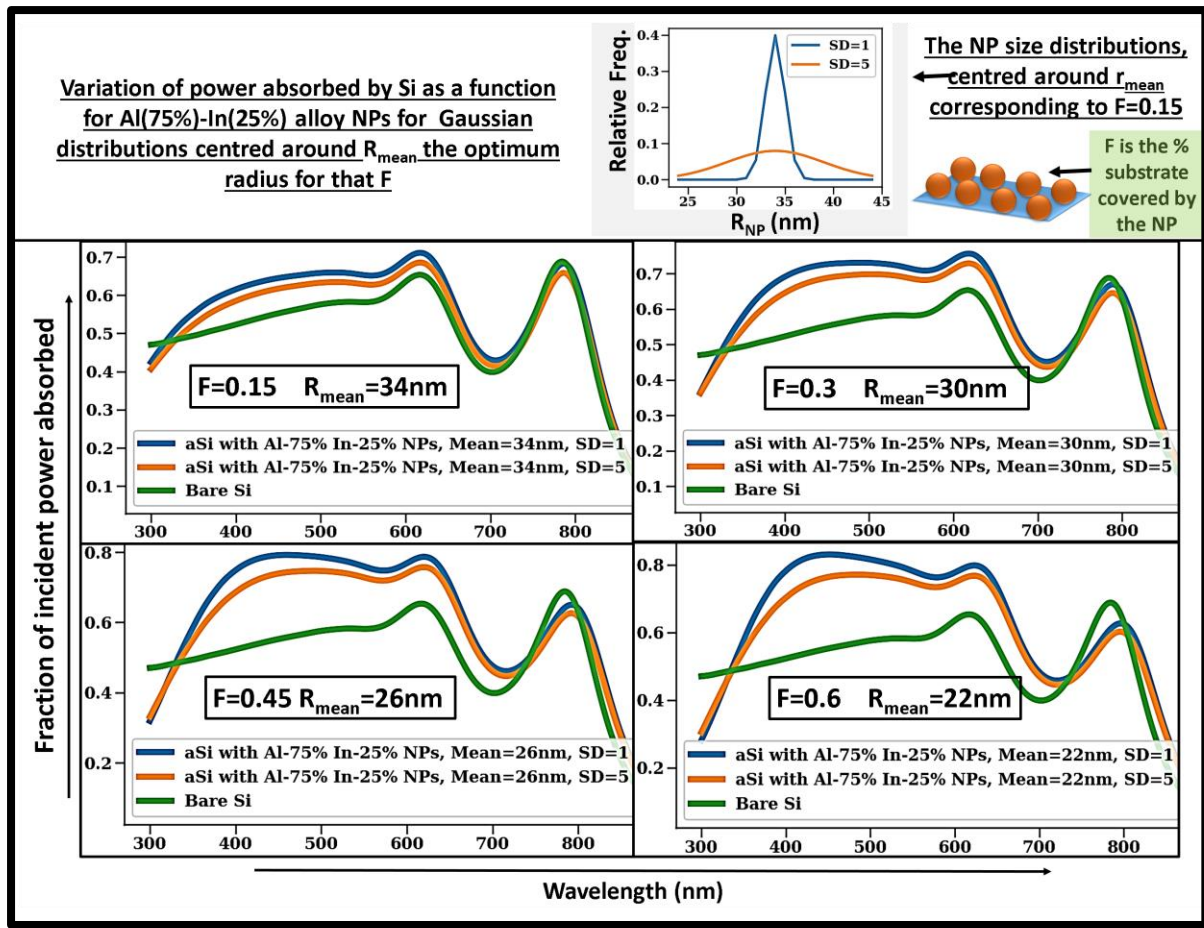


Figure 5-9. We consider Gaussian distributions of Al-In NP radii ($f_{\text{Al}}=75\%$), centred around the R_{optimum} for each value of the surface coverage, F . The distributions are shown in the inset figure. For $F=0.6$, for a narrow distribution ($\text{SD}=1$), an enhancement of 27% is seen vs bare a:Si. For a flatter distribution ($\text{SD}=5$), an enhancement of 21% is seen vs bare a:Si.

Since common NP synthesis techniques rarely produce size focussed nanoparticles, we consider NP size distributions, as shown in Figure 5-9. Two Gaussian size distributions are considered, with varying Standard Deviations (SD), centred around the R_{optimum} corresponding to the value of the surface coverage (F) used, with $\text{SD}=1$ (a steeper distribution) and $\text{SD}=5$ (a flatter distribution). The distributions are shown in the inset figure. When $F=0.6$, for a narrow distribution of Al-75% In-25% NPs ($f_{\text{Al}}=75\%$) (centred around $R=22\text{nm}$), there is a 27% increase in the weighted power absorbed by a:Si in the 300-900nm region, when compared to bare a:Si. For a broader distribution ($\text{SD}=5$) there is a 21% increase in the weighted power absorbed by a:Si in the 300-900nm region, when compared to bare a:Si. This shows that even a fairly wide distribution of particle sizes (span=20nm) can produce a significant increase in

the absorption of a:Si. This means that non-size focussed synthesis mechanisms, such as co-precipitation can be used for the synthesis of Al alloy NPs, as long as the mean radius can be controlled.

CHAPTER 6 : Summary and Conclusions

The presence of a copper shell on aluminum nanoparticles not only stabilizes it, but also significantly enhances its plasmonic properties. Cubical morphologies are shown to have a greater plasmonic response than spheres. A 100nm cube shows a 250% improvement in ABS and 175% improvement in SCS w.r.t a 100nm sphere at its scattering and absorption peaks. As the shell thickness increases, the absorption cross section of these particles increases.

Moreover, by changing the shell thickness, it is possible to engineer different positions for peak scattering and absorption. The peak absorption and scattering wavelengths show almost a linear increase with Cu shell thickness, and the design equations for the same have been provided. A 10nm Cu shell on a 100nm Al cube shifts the absorption peak from 375nm to 480nm and the scattering peak from 360nm to 660nm. This is accompanied by an 86% increase in peak absorption intensity and only a 11.5% decrease in peak scattering intensity, thus offering great design flexibility. Nanocuboids show orientation dependent plasmonic response. By changing the orientation, the absorption and scattering peaks can be positioned in the UV (200-360nm) or visible (400-700nm) region. While oxide layers of thickness up to 1nm may be expected, we show that for a 1nm oxide shell, the scattering and absorption cross sections are almost unchanged. Alloys of Al and Cu also show promise and show almost identical scattering curves as the Cu content is changed from 0% to 50%. Dimers of two cubes at an angle of 45 degrees show the highest absorption cross sections while dimers of two spheres of the same volume show the highest scattering cross sections, with the same interparticle distance.

Therefore, this study presents a comprehensive calculation of the effects of a Cu shell on the plasmonic properties of an Al nanoparticle. The addition of a Cu shell to Al represents an effective method to tap into the plasmonic properties of aluminum.

We have studied the plasmonic properties and light trapping efficiency of five types of Al nanoparticles: Al-Cu, Al-Au, Al-Ni, Al-In and Al-Mg. Al-In and Al-Mg alloy NPs are better scatterers of light with a weighted scattering ratio of 0.76 and 0.74 for 50% Al-Mg and Al-In alloy of radius 60nm, as opposed to 0.63, 0.71 and 0.7 values for Al-Cu, Al-Au and Al-Ni NPs.

We investigate the utility of these Al alloy NPs for light trapping in a thin film amorphous Si solar cell. We uncover the role that the surface coverage, F, plays in enhancing light trapping. For every F, there exists an optimum value (r_{optimum}) of the NPs used, and r_{optimum} decreases with increasing F. For example, when $F=0.4$, $r_{\text{optimum}}=22\text{nm}$, but when $F=0.1$, $r_{\text{optimum}}=34\text{nm}$.

Al-In and Al-Mg alloys emerge as the best candidates for light trapping applications in thin film solar cells. When $F=0.6$, and $r_{\text{NP}}=r_{\text{optimum}}=22\text{nm}$, Al(75%)-Mg(25%) and Al(75%)-In(25%) alloys improve the absorption of aSi by 28%. Additionally, we find that pure Al NP and Ag NPs of the same size cause a 29% and 13% enhancement, respectively in the absorption of aSi. Thus, alloying Al with metals like Al can improve their corrosion stability without having a deleterious effect on their light trapping efficiency. Al-based plasmonics also show superior performance to noble metal plasmonics.

We also show that a distribution of particle sizes can also improve the light trapping efficiency. For example, for $F=0.6$, a Gaussian distribution of Al_3In particle sizes (standard deviation=5) around $r_{\text{mean}}=22\text{nm}$ improves the absorption of amorphous silicon by 21%.

Thus, this study reports Al-alloy nanoparticles, particularly Al-In and Al-Mg NPs high Al content as effective for plasmonic light trapping applications. Thus Al-alloys offer significant utility for plasmonic light trapping, whilst offering a degree of environmental robustness not offered by pure Al NPs. As the synthesis of Al-alloy NPs is well defined in literature, it is

hoped that this report will spur further work in the hitherto unexplored world of Al-alloy plasmonics.

It is believed that results reported here, provide a reasonable avenue for enabling scalable, low-cost plasmonic technologies.

Prospects Generated by this Work:

1. While nanocubes and nanocuboids have shown excellent promise for plasmonic applications, their controlled synthesis remains problematic. This creates an opportunity for fresh impetus in this area, particularly due to their promising plasmonic properties
2. Effective Medium Theory has been shown to be a quick, computationally efficient and accurate method to study multilayer stacks of thin films which has particular promise for solar cell applications. However, current effective medium theories can only handle a suspension of metallic spheres inside a dielectric. There is a possibility, by introducing suitable correction factors to account for facetedness, these theories could be used to study the optical properties of nanocubes and nanocuboids in a dielectric medium
3. Effective Medium Theories are not accurate for core-shell nanoparticles, making the study of the oxidation effects on these nanoparticles difficult. However, it is quite possible to generate “Inverse Mie Functions” for core-shell nanoparticles. For example, the absorption and scattering spectra of core-shell nanoparticles can be easily obtained. It is also possible to create an equivalent sphere from the absorption and scattering spectra generated from the core-shell nanoparticle, which has the same radius, different n, k values but is homogeneous, i.e does not have a shell. The study of this “equivalent sphere” becomes much easier, especially in effective medium theories.
4. Cermets are promising for photothermal applications. Using a combination of Bruggeman’s Formula and heat transfer equations, the temperature rise for different cermet NP-nanofluids can be found
5. It is also worthwhile to study the plasmonic properties of intermetallic NPs, however the optical constants need to be calculated using first principle calculations.
6. Finally, it is possible to use neural networks, effective medium theories and transfer matrix models to create the “perfect solar cell” in an exercise of materials discovery

Recommendations for Future Work:

1. More experimental insights into tuning the core, shell and particle sizes as well as alloy compositions is needed to further this work
2. Extension of the Effective Medium Theory to consider plasmon hybridization effects. This will make effective medium theories more robust and accurate for studying the optical properties of a multilayer stack of thin films.

Papers Resulting from This Work

1. "Al-Cu core-shell nanoparticles as an alternative to noble metal plasmonics: A Computational Study", Arvind Pujari and Tiju Thomas, *Materials Chemistry and Physics* (2020), doi: <https://doi.org/10.1016/j.matchemphys.2020.123419>
2. Al-alloy Nanoparticles for Improved Plasmonic Light Trapping in Thin Film Solar Cells: A Computational Study, Arvind Pujari and Tiju Thomas, *Manuscript Under Preparation*

Patents Resulting from This Work

1. Arvind Pujari and Tiju Thomas, "Al-Cu core-shell nanoparticles with tunable optical spectra", Application No. 201941050328, Indian Patent (2019)
2. Tandem grey water reactors based on non-noble plasmonics and BaTaO_{2-x}Ny /CuO quantum dot heterostructure based photocatalysts, IDF No. 2018

References

- [1] V. E. Ferry *et al.*, "Light trapping in ultrathin plasmonic solar cells," *Opt. Express*, vol. 18, no. S2, p. A237, Jun. 2010, doi: 10.1364/oe.18.00a237.
- [2] K. R. Catchpole and A. Polman, "Plasmonic solar cells," *Opt. Express*, vol. 16, no. 26, p. 21793, Dec. 2008, doi: 10.1364/oe.16.021793.

- [3] J. Song, J. Zhou, and H. Duan, “Self-assembled plasmonic vesicles of SERS-encoded amphiphilic gold nanoparticles for cancer cell targeting and traceable intracellular drug delivery,” *J. Am. Chem. Soc.*, vol. 134, no. 32, pp. 13458–13469, Aug. 2012, doi: 10.1021/ja305154a.
- [4] X. Wu *et al.*, “Reports on Progress in Physics Plasmonic photocatalysis Direct photocatalysis of supported metal nanostructures for organic synthesis Photocatalytic composites based on titania nanoparticles and carbon nanomaterials Plasmonic photocatalysis,” *Rep Prog Phys*, vol. 76, pp. 46401–41, 2013, doi: 10.1088/0034-4885/76/4/046401.
- [5] T. Liu and Y. Li, “Photocatalysis: Plasmonic solar desalination,” *Nature Photonics*, vol. 10, no. 6. Nature Publishing Group, pp. 361–362, Jun. 01, 2016, doi: 10.1038/nphoton.2016.97.
- [6] E. Ozbay, “Plasmonics: Merging photonics and electronics at nanoscale dimensions,” *Science*, vol. 311, no. 5758. pp. 189–193, Jan. 13, 2006, doi: 10.1126/science.1114849.
- [7] Y. Huang, L. Wu, || Xiaodong Chen, P. Bai, and D.-H. Kim, “Synthesis of Anisotropic Concave Gold Nanocuboids with Distinctive Plasmonic Properties,” 2013, doi: 10.1021/cm400765b.
- [8] A. Bottomley and A. Ianoul, “Reflection and Absorption Spectra of Silver Nanocubes on a Dielectric Substrate: Anisotropy, Angle, and Polarization Dependencies,” 2014, doi: 10.1021/jp508629d.
- [9] W. Li *et al.*, “Aluminum nanopyramid array with tunable ultraviolet-visible-infrared wavelength plasmon resonances for rapid detection of carbohydrate antigen 199,” *Biosens. Bioelectron.*, vol. 79, pp. 500–507, May 2016, doi: 10.1016/j.bios.2015.12.038.

- [10] G. V. Naik, V. M. Shalaev, and A. Boltasseva, “Alternative plasmonic materials: Beyond gold and silver,” *Advanced Materials*, vol. 25, no. 24. pp. 3264–3294, Jun. 25, 2013, doi: 10.1002/adma.201205076.
- [11] D. Gérard and S. K. Gray, “Special issue on aluminium plasmonics,” *Journal of Physics D: Applied Physics*, vol. 48, no. 18. Institute of Physics Publishing, May 13, 2015, doi: 10.1088/0022-3727/48/18/180301.
- [12] M. W. Knight, N. S. King, L. Liu, H. O. Everitt, P. Nordlander, and N. J. Halas, “Aluminum for Plasmonics,” vol. 41, p. 30, 2019, doi: 10.1021/nn405495q.
- [13] N. P. Hylton *et al.*, “Loss mitigation in plasmonic solar cells: Aluminium nanoparticles for broadband photocurrent enhancements in gaas photodiodes,” *Sci. Rep.*, vol. 3, 2013, doi: 10.1038/srep02874.
- [14] L. Zhou *et al.*, “3D self-assembly of aluminium nanoparticles for plasmon-enhanced solar desalination,” *Nat. Photonics*, vol. 10, no. 6, pp. 393–398, Jun. 2016, doi: 10.1038/nphoton.2016.75.
- [15] W. F. Bogaerts and C. M. Lampert, “Review Materials for photothermal solar energy conversion,” 1983.
- [16] D. Gerard and S. K. Gray, “Aluminium plasmonics,” *J. Phys. Appl. Phys.*, vol. 48, no. 18, May 2015, doi: 10.1088/0022-3727/48/18/184001.
- [17] A. G. Brolo, “Plasmonics for future biosensors,” *Nat. Photonics*, vol. 6, no. 11, pp. 709–713, Nov. 2012, doi: 10.1038/nphoton.2012.266.
- [18] J. Leuthold *et al.*, “Plasmonic Communications: Light on a Wire,” *Opt. Photonics News*, vol. 24, no. 5, pp. 28–35, May 2013, doi: 10.1364/OPN.24.5.000028.
- [19] X. Huang, P. K. Jain, I. H. El-Sayed, and M. A. El-Sayed, “Plasmonic photothermal therapy (PPTT) using gold nanoparticles,” *Lasers Med. Sci.*, vol. 23, no. 3, p. 217, Aug. 2007, doi: 10.1007/s10103-007-0470-x.

- [20] “OSA | Plasmonic solar cells.” <https://www.osapublishing.org/oe/abstract.cfm?uri=oe-16-26-21793> (accessed May 19, 2020).
- [21] L. Liu *et al.*, “Gold photosensitized SrTiO₃ for visible-light water oxidation induced by Au interband transitions,” *J. Mater. Chem. A*, vol. 2, no. 25, pp. 9875–9882, Jun. 2014, doi: 10.1039/C4TA01988A.
- [22] V. J. Keast, T. A. Myles, N. Shahcheraghi, and M. B. Cortie, “Corrosion processes of triangular silver nanoparticles compared to bulk silver,” *J. Nanoparticle Res.*, vol. 18, no. 2, p. 45, Feb. 2016, doi: 10.1007/s11051-016-3354-9.
- [23] M. W. Knight, N. S. King, L. Liu, H. O. Everitt, P. Nordlander, and N. J. Halas, “Aluminum for Plasmonics,” *ACS Nano*, vol. 8, no. 1, pp. 834–840, Jan. 2014, doi: 10.1021/nn405495q.
- [24] V. V. Temnov, “Ultrafast acousto-magneto-plasmonics,” *Nat. Photonics*, vol. 6, no. 11, pp. 728–736, Nov. 2012, doi: 10.1038/nphoton.2012.220.
- [25] Q.-C. Sun, Y. Ding, S. M. Goodman, H. H. Funke, and P. Nagpal, “Copper plasmonics and catalysis: role of electron–phonon interactions in dephasing localized surface plasmons,” *Nanoscale*, vol. 6, no. 21, pp. 12450–12457, Oct. 2014, doi: 10.1039/C4NR04719B.
- [26] S. Kim, J.-M. Kim, J.-E. Park, and J.-M. Nam, “Non noble-Metal-Based Plasmonic Nanomaterials: Recent Advances and Future Perspectives,” *Adv. Mater.*, vol. 30, no. 42, p. 1704528, Oct. 2018, doi: 10.1002/adma.201704528.
- [27] “Magnesium Nanoparticle Plasmonics | Nano Letters.” <https://pubs.acs.org/doi/abs/10.1021/acs.nanolett.8b00955> (accessed May 19, 2020).
- [28] “Localized Surface Plasmon Resonances in Aluminum Nanodisks | Nano Letters.” <https://pubs.acs.org/doi/abs/10.1021/nl080453i> (accessed May 19, 2020).

- [29] R. Y. Koyama, N. V. Smith, and W. E. Spicer, “Optical Properties of Indium,” *Phys. Rev. B*, vol. 8, no. 6, pp. 2426–2432, Sep. 1973, doi: 10.1103/PhysRevB.8.2426.
- [30] “The optical properties and electronic structure of magnesium - IOPscience.” <https://iopscience.iop.org/article/10.1088/0370-1328/92/4/316/meta> (accessed May 19, 2020).
- [31] S. Babar and J. H. Weaver, “Optical constants of Cu, Ag, and Au revisited,” *Appl. Opt.*, vol. 54, no. 3, pp. 477–481, Jan. 2015, doi: 10.1364/AO.54.000477.
- [32] “Plasmonic light trapping in thin-film Si solar cells - IOPscience.” <https://iopscience.iop.org/article/10.1088/2040-8978/14/2/024002/meta> (accessed May 19, 2020).
- [33] A. Shah *et al.*, “Towards very low-cost mass production of thin-film silicon photovoltaic (PV) solar modules on glass,” *Thin Solid Films*, vol. 502, no. 1, pp. 292–299, Apr. 2006, doi: 10.1016/j.tsf.2005.07.299.
- [34] D. E. Carlson and C. R. Wronski, “Amorphous silicon solar cell,” *Appl. Phys. Lett.*, vol. 28, no. 11, pp. 671–673, Jun. 1976, doi: 10.1063/1.88617.
- [35] W. M. Cheung, C. F. Cheng, M. C. Poon, C. W. Kok, and M. Chan, “Amorphous silicon deposition temperature optimization on advanced polysilicon thin-film formation using metal-induced lateral crystallization technology,” in *Proceedings 2002 IEEE Hong Kong Electron Devices Meeting (Cat. No.02TH8616)*, Jun. 2002, pp. 27–30, doi: 10.1109/HKEDM.2002.1029149.
- [36] M. Stuckelberger, M. Despeisse, G. Bugnon, J.-W. Schüttauf, F.-J. Haug, and C. Ballif, “Comparison of amorphous silicon absorber materials: Light-induced degradation and solar cell efficiency,” *J. Appl. Phys.*, vol. 114, no. 15, p. 154509, Oct. 2013, doi: 10.1063/1.4824813.

- [37] H. Tan, R. Santbergen, A. H. M. Smets, and M. Zeman, “Plasmonic Light Trapping in Thin-film Silicon Solar Cells with Improved Self-Assembled Silver Nanoparticles,” *Nano Lett.*, vol. 12, no. 8, pp. 4070–4076, Aug. 2012, doi: 10.1021/nl301521z.
- [38] F. J. Beck, S. Mokkapati, and K. R. Catchpole, “Plasmonic light-trapping for Si solar cells using self-assembled, Ag nanoparticles,” *Prog. Photovolt. Res. Appl.*, vol. 18, no. 7, pp. 500–504, 2010, doi: 10.1002/pip.1006.
- [39] “Exceeding the limit of plasmonic light trapping in textured screen-printed solar cells using Al nanoparticles and wrinkle-like graphene sheets | Light: Science & Applications.” <https://www.nature.com/articles/lsta201348> (accessed May 19, 2020).
- [40] H. R. Ghorbani, “A Review of Methods for Synthesis of Al Nanoparticles,” *Orient. J. Chem.*, vol. 30, no. 4, pp. 1941–1949, Dec. 2014.
- [41] N. Arora and B. R. Jagirdar, “Monodispersity and stability: case of ultrafine aluminium nanoparticles (<5 nm) synthesized by the solvated metal atom dispersion approach,” *J. Mater. Chem.*, vol. 22, no. 18, pp. 9058–9063, Apr. 2012, doi: 10.1039/C2JM16764F.
- [42] N. V. Svarovskaya *et al.*, “Chemical behaviour of Al/Cu nanoparticles in water,” *Prog. Nat. Sci. Mater. Int.*, vol. 25, no. 1, pp. 1–5, Feb. 2015, doi: 10.1016/j.pnsc.2015.01.001.
- [43] F. Noor, A. Vorozhtsov, M. Lerner, E. P. Bandarra Filho, and D. Wen, “Thermal- Chemical Characteristics of Al–Cu Alloy Nanoparticles,” *J. Phys. Chem. C*, p. 150616125001008, Jun. 2015, doi: 10.1021/acs.jpcc.5b01515.
- [44] N. Patra, R. Patil, A. Sharma, V. Singh, and I. A. Palani, “Comparative study on Cu, Al and Cu-Al alloy nanoparticles synthesized through underwater laser ablation technique,” *IOP Conf. Ser. Mater. Sci. Eng.*, vol. 390, p. 012046, Jul. 2018, doi: 10.1088/1757-899X/390/1/012046.

- [45] Z. Wang, A. L. Fan, W. H. Tian, Y. T. Wang, and X. G. Li, “Synthesis and structural features of Ni–Al nanoparticles by hydrogen plasma–metal reaction,” *Mater. Lett.*, vol. 60, no. 17, pp. 2227–2231, Aug. 2006, doi: 10.1016/j.matlet.2005.12.116.
- [46] S. Z. E. Abedin and F. Endres, “Electrochemical Behaviour of Al, Al–In and Al–Ga–In Alloys in Chloride Solutions Containing Zinc Ions,” *J. Appl. Electrochem.*, vol. 34, no. 10, pp. 1071–1080, Oct. 2004, doi: 10.1023/B:JACH.0000042672.23588.df.
- [47] “Synthesis of Stable Al(0) Nanoparticles in Water in the form of Al(0)@Cu and Sequestration of Cu²⁺(aq) with Simultaneous H₂ Production | ACS Sustainable Chemistry & Engineering.” <https://pubs.acs.org/doi/abs/10.1021/acssuschemeng.9b00340> (accessed May 19, 2020).
- [48] T. P. Yadav, R. M. Yadav, and D. P. Singh, “Mechanical Milling: a Top Down Approach for the Synthesis of Nanomaterials and Nanocomposites,” *Nanosci. Nanotechnol.*, vol. 2, no. 3, pp. 22–48, 2012.
- [49] Y. A. Akimov and W. S. Koh, “Design of Plasmonic Nanoparticles for Efficient Subwavelength Light Trapping in Thin-Film Solar Cells,” *Plasmonics*, vol. 6, no. 1, pp. 155–161, Mar. 2011, doi: 10.1007/s11468-010-9181-4.
- [50] J. P. Berenger, “A perfectly matched layer for the absorption of electromagnetic waves,” *J. Comput. Phys.*, vol. 114, no. 2, pp. 185–200, 1994, doi: 10.1006/jcph.1994.1159.
- [51] P. B. Johnson and R. W. Christy, “Optical constants of the noble metals,” *Phys. Rev. B*, vol. 6, no. 12, pp. 4370–4379, 1972, doi: 10.1103/PhysRevB.6.4370.
- [52] A. P. Lenham and D. M. Treherne, “The optical constants of aluminium and indium,” *Proc. Phys. Soc.*, vol. 85, no. 1, pp. 167–170, 1965, doi: 10.1088/0370-1328/85/1/324.
- [53] N. R. Dhineshbabu, V. Rajendran, N. Nithyavathy, and R. Vetumperumal, “Study of structural and optical properties of cupric oxide nanoparticles,” *Appl. Nanosci. Switz.*, vol. 6, no. 6, pp. 933–939, Aug. 2016, doi: 10.1007/s13204-015-0499-2.

- [54] D. J. Bergman, “The dielectric constant of a composite material-A problem in classical physics,” *Physics Reports*, vol. 43, no. 9, pp. 377–407, 1978, doi: 10.1016/0370-1573(78)90009-1.
- [55] C. F. Bohren and D. R. Huffman, *Absorption and scattering of light by small particles*. New York: Wiley, 1983.
- [56] B. J. Sumlin, W. R. Heinson, and R. K. Chakrabarty, “Retrieving the aerosol complex refractive index using PyMieScatt: A Mie computational package with visualization capabilities,” *J. Quant. Spectrosc. Radiat. Transf.*, vol. 205, pp. 127–134, Jan. 2018, doi: 10.1016/j.jqsrt.2017.10.012.
- [57] D. Alonso-Álvarez, T. Wilson, P. Pearce, M. Führer, D. Farrell, and N. Ekins-Daukes, “Solcore: a multi-scale, Python-based library for modelling solar cells and semiconductor materials,” *J. Comput. Electron.*, vol. 17, no. 3, pp. 1099–1123, Sep. 2018, doi: 10.1007/s10825-018-1171-3.
- [58] A. D. Rakić, “Algorithm for the determination of intrinsic optical constants of metal films: application to aluminum,” *Appl. Opt.*, vol. 34, no. 22, pp. 4755–4767, Aug. 1995, doi: 10.1364/AO.34.004755.
- [59] P. B. Johnson and R. W. Christy, “Optical Constants of the Noble Metals,” *Phys. Rev. B*, vol. 6, no. 12, pp. 4370–4379, Dec. 1972, doi: 10.1103/PhysRevB.6.4370.
- [60] A. G. Mathewson and H. P. Myers, “Absolute Values of the Optical Constants of Some Pure Metals,” *Phys. Scr.*, vol. 4, no. 6, pp. 291–292, Dec. 1971, doi: 10.1088/0031-8949/4/6/009.
- [61] H.-J. Hagemann, W. Gudat, and C. Kunz, “Optical constants from the far infrared to the x-ray region: Mg, Al, Cu, Ag, Au, Bi, C, and Al_2O_3 ,” *JOSA*, vol. 65, no. 6, pp. 742–744, Jun. 1975, doi: 10.1364/JOSA.65.000742.

- [62] T. C. Choy, *Effective medium theory: principles and applications*, Second edition. Oxford: Oxford University Press, 2016.
- [63] “Phys. Rev. B 5, 3017 (1972) - Electronic Structure of Amorphous Si from Photoemission and Optical Studies.” <https://journals.aps.org/prb/abstract/10.1103/PhysRevB.5.3017> (accessed May 17, 2020).
- [64] T. A. F. König *et al.*, “Electrically Tunable Plasmonic Behavior of Nanocube–Polymer Nanomaterials Induced by a Redox-Active Electrochromic Polymer,” *ACS Nano*, vol. 8, no. 6, pp. 6182–6192, Jun. 2014, doi: 10.1021/nn501601e.
- [65] S. J. Byrnes, “Multilayer optical calculations,” *ArXiv160302720 Phys.*, Nov. 2019, Accessed: May 17, 2020. [Online]. Available: <http://arxiv.org/abs/1603.02720>.
- [66] W. T. Doyle, “Optical properties of a suspension of metal spheres,” *Phys. Rev. B*, vol. 39, no. 14, pp. 9852–9858, May 1989, doi: 10.1103/PhysRevB.39.9852.
- [67] M. Alsawafta, M. Wahbeh, and V.-V. Truong, “Simulated Optical Properties of Gold Nanocubes and Nanobars by Discrete Dipole Approximation,” *J. Nanomater.*, vol. 2012, 2012, doi: 10.1155/2012/283230.
- [68] M. D. Skarlinski and D. J. Quesnel, “Effect of native oxide layers on copper thin-film tensile properties: A reactive molecular dynamics study,” *Cit. J Appl Phys*, vol. 118, p. 235306, 2015, doi: 10.1063/1.4938384.
- [69] A. Ravirajan, A. Umasankaran, and T. Thomas, “Al-In nanoparticles and their clusters as solar spectrum plasmonic resonators,” *Mater. Sci. Eng. B Solid-State Mater. Adv. Technol.*, vol. 242, pp. 75–82, Mar. 2019, doi: 10.1016/j.mseb.2019.03.011.